Quantification of DNA content using 3D Optical Projection Tomographic Microscopy for Early Cancer Diagnosis

Nitin Agarwal

A thesis submitted in partial fulfilment of the
requirements for the degree of

Master of Science

University of Washington
2013

Committee
Eric J. Seibel, PhD
Matthew O'Donnell, PhD

Program Authorized to Offer Degree
Department of Bioengineering

University of Washington

Abstract

Quantification of DNA content using 3D Optical Projection Tomographic Microscopy for Early Cancer Diagnosis

Nitin Agarwal

Chair of the Supervisory Committee:
Eric J. Seibel, Research Professor
Mechanical Engineering

Aneuploidy, an accepted biomarker for malignancy, is typically assessed by flow (FCM) and image cytometry (ICM). We used optical projection tomographic microscopy (OPTM) for assessing cellular DNA content using different absorption and fluorescence stains. OPTM combines some attributes of both FCM and ICM and provides quantitative cytometry with 3D visualization of morphology. It generates submicron, isometric three-dimensional (3D) images of nuclear features, performing multimodal imaging with exact co-registration. We further present a novel automated method for 3D nucleus segmentation. First, nuclei of chicken erythrocyte, trout erythrocyte and triploid trout erythrocyte standards were used to calibrate the OPTM for stoichiometric DNA ploidy assessment. Thionin, as an alternative to Feulgen stain was optimized for stoichiometry by varying the staining time. DNA indices were extracted from 50 images of each standard and their ratios were compared to FCM. A similar comparison was done with hematoxylin, Feulgen and sytox green labeling. The mean square error (MSE) of the three ratios was highest with hematoxylin and least with Feulgen. Forty-five minutes (45mins) of thionin staining time had least MSE among different thionin stains. Sytox green MSE was greater than

both thionin and Feulgen but less than hematoxylin. For all three ratios, variance of hematoxylin was significantly greater than 45min thionin, which was greater than Feulgen ($p<0.01$). The variance of sytox green was significantly greater than Feulgen but not less than 45min thionin ($p>0.01$). From qualitative assessment of seven cancer cell lines, morphology was preserved only for hematoxylin and Feulgen stain. Thus, Feulgen stain, like in 2D analysis, is stoichiometric with least variance while also preserving nuclear morphology in 3D. We further tested feulgen stain on seven different cancer cell lines for DNA index. We compared our results with FCM and obtained an agreement on five cancer cell lines. The possible reason for discrepancies in two cancer cell lines could be due to inaccurate three-dimensional segmentation. In conclusion we present a novel technique for quantitative measurement of DNA content, while preserving the nuclear morphology in 3D. The addition of this quantitative biomarker could further strengthen existing classifiers and improve early diagnosis of cancer using 3D microscopy.

UW Graduate School
Master's Supervisory Committee Approval Form

Student Instructions

- Complete all fields on this form. Names must match what is on your title page and information must match what you entered in the UW ETD Administrator Site.
- Obtain *original* (ink) signatures – no faxes, scans, stamps, emails.
- Your *signed* form may be delivered in person, or by campus or postal mail, and must be received by 5:00 p.m. PST on the last day of the quarter.

  University of Washington
  Graduate Enrollment Management Services (GEMS)
  G-1 Communications, Box 353770
  Seattle, WA 98195-3770
- GEMS will not be able to review your submission in the UW ETD Administrator Site or approve your thesis and process your graduation until your *signed* form has been received.
- If your form is incomplete (missing information and/or signatures) or if GEMS receives it after 5:00 p.m. PST on the last day of the quarter, you will be required to register the following quarter or pay the $250 Graduate Registration Waiver Fee: http://www.grad.washington.edu/policies/general/regwaiver.shtml

Student Information

Student Name: NITIN AGARWAL
Student ID #: 1121124
Quarter/Year Graduation: AUTUMN/2013
UW Email Account: agarwaln@uw.edu
Name of Degree: Master of Science
Program: Bioengineering

Student Agreement

I certify that I have presented my master's supervisory committee with the final copy of my master's thesis for examination and approval.

Signature of Student: Nagarwal Date: 08/23/2013

Master's Supervisory Committee Agreement

I certify that I have examined the final copy of the above student's master's thesis and have found that it is complete and satisfactory in all respects, and that any and all revisions required by the final examining committee have been made.

Signature of Committee Chair: Date: 08/23/2013
Print name below line signature line: Prof Eric J. Seibel

Signature of Committee Co-Chair (if applicable): Date:
Print name below signature line:

Signature of Committee Member: Date: 08/23/2013
Print name below signature line: Prof Mathew O'Donnell

Signature of Committee Member: Date:
Print name below signature line:

Signature of Committee Member: Date:
Print name below signature line:

Questions: Please contact Graduate Enrollment Management Services (GEMS) at uwgrad@uw.edu or 206.685.2630.

Acknowledgements

I would like to express my sincere gratitude to Dr Eric Seibel, who gave me the opportunity to work in this interesting area of biomedical imaging, and for his continuous support and encouragement. I would also like to thank Dr Anthony Reeves and Dr Alberto Biancardi for assistance with 3D image processing. Thanks to Dr Alan Nelson for proving the Cell-CT and making this research possible. I would also like to thank Sarah Shimer, Ben Hawthorne, Yuriana Garcia, Florence Patten, Anna Tourovskaia, Greg Kramer, Elizabeth Asp, Ryland Bryant, Mathew Watson, Christy Lancaster, David Steinhauer, Jon Hayenga, Michael Meyer, Rahul Katdare for their technical support and assistance with sample preparation.

Special thanks to Charles Mahan, Kelly Hudkins, Donna Prunkard, and Dr Peter Rabinovitch of Dept. of Pathology at University of Washington-Seattle for providing assistance with staining and flow cytometry. Thanks to Biosure and ATCC for providing all the flow cytometry internal standards and cultured cancer cells. I would also like to thank Richard Johnston, David Melville and all the other members of the human photonics laboratory for their insightful discussions and support. This collaborative research was made possible by funding from National Science Foundation (CBET-1014976 & 1014813). Last but not the least, I would like to thank my parents and family for their continuous love, encouragement and blessings.

Dedication

To My Family

Table of Contents

Abstract……..... iii

Acknowledgements…….. vi

Table of Contents…….. viii

List of Figures……... xi

List of Tables……. xvi

List of Abbreviations…… xvii

Chapter 1. Background and Significance…….. 1

1.1 What is Cancer?..... 1

1.2 Current techniques for cancer diagnosis..... 2

1.3 Aneuploidy, a biomarker for cancer diagnosis..... 3

1.4 Current techniques for aneuploidy measurement..... 4

1.4.1 Flow cytometry**……..... 5**

1.4.2 2D Image Cytometry**..... 6**

1.5 Research Objective..... 8

Chapter 2 Existing 3D Microscopes..... 9

2.1 Optical Coherence Tomography……..... 10

2.2 Photoacoustic Tomography……..... 10

2.3 Confocal Microscopy..... 11

Chapter 3. Optical Projection Tomographic Microscopy (OPTM)..... 13

3.1 Introduction..... 13

3.2 Construction..... 16

3.3 Image acquisition..... 18

3.4 Image reconstruction..... 18

3.5 3D Segmentation..... 18

Chapter 4. Calibrating OPTM for stoichiometry DNA ploidy analysis……..... 24

4.1 Sample preparation……..... 24

4.2 Flow cytometry..... 25

4.3 3D Image cytometry..... 25

4.3.1 Acidic thionin staining..... **26**

4.3.2 Hematoxylin staining..... **26**

4.3.3 Feulgen staining..... **27**

4.3.4 Sytox green staining..... **27**

4.4 DNA content analysis..... 28

4.5 Results and Discussion..... 29

4.5.1 Stoichiometry..... **31**

4.5.2 Variability..... **32**

4.5.3 Morphology..... **32**

4.5 Conclusion..... 36

Chapter 5. Testing stoichiometric DNA ploidy analysis with different cancer cell line 37

5.1 Sample Preparation..... 38

5.2 Flow Cytometry..... 38

5.3 3D Image Cytometry..... 39

5.4 Results and Discussion..... 39

5.4.1 DNA index (DI) **..... 39**

5.4.2 S-Phase fraction (SPF) **..... 47**

5.4.3 Morphology**..... 47**

5.5 Conclusion..... 49

Chapter 6. Future directions and Conclusion..... 51

6.1 Clinical Impact..... 51

6.2 Improved OPTM..... 52

6.3 Improved 3D segmentation..... 53

6.4 Tissue Biopsies Analysis..... 55

6.5 Conclusion..... 55

List of references..... 57

List of Figures

Figure 1. Cell cycle of a cancer cell **4**

Figure 2. FACSAria™ III from Becton Dickinson **6**

Figure 3. EVOS® FL auto cell-imaging system from Invitrogen **7**

Figure 4. Basic setup of an optical projection tomographic microscopy (OPTM) **14**

Figure 5. Sensitivity versus number of features: 96% specificity. Shown are average sensitivities for 3D (blue) and 2D (red). **15**

Figure 6. Schematic diagram on an OPTM. **17**

Figure 7. Central slice of a cell showing agreement of manual markings (cyan and yellow) with that obtained from computer using image threshold (green and red). **19**

Figure 8. 3D segmentation of an A549 stained with feulgen stain. (A). Histogram and (B). Merit function (M_i) of the central slice (I_c) of the image across the same range of intensity values. (C). Central slice of A549 cell with first peak used as the threshold (D). Central slice of A549 cell with both the peaks used as the threshold. 3D surface rendering of (E). axial, (F). sagittal and (G). coronal views of A549 cell computed by applying automatically determined thresholds to the whole 3D image. **22**

Figure 9. 3D segmentation of TTEN stained with 45min acidic thionin stain. (A). Histogram and (B). Merit function (M_i) of the central slice (I_c) of the nuclei image across the same range of intensity values. (C). Central slice of TTEN nucleus image (D). Central slice of TTEN nuclear region with the first peaks used as the threshold. 3D surface rendering of (E). axial, (F). sagittal and (G). coronal views of TTEN nuclear region computed by applying automatically determined threshold to the whole 3D image. **23**

Figure 10. Diagram showing the three internal standards along with acidic thionin stain. **25**

Figure 11. 3D renderings of the axial view of a TEN stained with (A). hematoxylin, (B). 15min thionin, (C). 30min thionin, (D). 45min thionin, (E). Feulgen and (F). sytox green. **29**

Figure 12. (A). The mean and the standard deviation of 50 ratios of individual observations for hematoxylin, sytox green and Feulgen stain along with ratios of DNA indices obtained from FCM. (B). The mean and the standard deviation of 50 ratios of individual observations for different thionin staining times along with ratios of DNA indices obtained from FCM. **30**

Figure 13: The MSE and its standard deviation along with 95% confidence interval of different stains. **31**

Figure 14. 3D visualization of morphology for three different A549 cancer cells stained with feulgen stain. **33**

Figure 15. 3D visualization of morphology for three different A549 cancer cells stained with hematoxylin stain. **33**

Figure 16. 3D visualization of morphology for three different A549 cancer cells stained with acidic thionin stain having a staining time of 45 minutes. **34**

Figure 17. 3D visualization of morphology for three different SKBR3 cancer cells stained with acidic thionin stain having a staining time of 30 seconds. **34**

Figure 18. Comparison of histograms of PC3 from FCM and OPTM. Histogram from FCM contains both lymphocytes and cancer cells, while histogram from OPTM only has cancer cells. There was a good correlation between both the histograms as most of the cancer cells were concentrated around 4c region. The small green peak and the blue peak following the 4c in the FCM histogram corresponds to the S phase and the G2 phase of the tumour population. **40**

Figure 19. Comparison of histograms of HT29 from FCM and OPTM. Histogram from FCM contains both lymphocytes and cancer cells, while histogram from OPTM only has cancer cells. There was a good correlation between both the histograms as most of the cancer cells were concentrated after 4c region. The small green peak following aneuploidy peak in the FCM histogram corresponds to the S phase of the tumour population. **40**

Figure 20. Comparison of histograms of HepG2 from FCM and OPTM. Histogram from FCM contains both lymphocytes and cancer cells, while histogram from OPTM only has cancer cells. There was a good correlation between both the histograms as most of the cancer cells were concentrated before 4c region. The small green peak and the blue peak following aneuploidy peak in the FCM histogram corresponds to the S phase and G2 phase of the tumour population. **41**

Figure 21. Comparison of histograms of CaCO2 from FCM and OPTM. Histogram from FCM contains both lymphocytes and cancer cells, while histogram from OPTM only has cancer cells. There was a good correlation between both the histograms as most of the cancer cells were concentrated at 6c region. The small green peak following aneuploidy peak in the FCM histogram corresponds to the S phase of the tumour population. **41**

Figure 22. Comparison of histograms of SKBR3 from FCM and OPTM. Histogram from FCM contains both lymphocytes and cancer cells, while histogram from OPTM only has cancer cells. There was a good correlation between both the histograms as most of the cancer cells were concentrated after 4c region. The green peak following aneuploidy peak in the FCM histogram was removed for better visualization of the aneuploidy peak with lymphocytes. **42**

Figure 23. Comparison of histograms of A549 from FCM and OPTM. Histogram from FCM contains both lymphocytes and cancer cells, while histogram from OPTM only has cancer cells. There was not a good correlation between both the histograms as the aneuploidy peak in FCM histogram lied between 2c and 4c while the peak in histogram from OPTM was near 4c. The small green peak following aneuploidy peak **42**

in FCM histogram corresponds to the S phase of the tumour population.

Figure 24. Comparison of histograms of BT474 from FCM and OPTM. Histogram from FCM contains both lymphocytes and cancer cells, while histogram from OPTM only has cancer cells. There was not a good correlation between both the histograms as the aneuploidy peak in FCM histogram was at 6c while the peak in histogram from OPTM was between 4c and 6c. The green peak following aneuploidy peak in FCM histogram was removed for better visualization of the tumour peak along with lymphocytes. **43**

Figure 25. A comparison of DNA indices of seven different cancer cell lines from FCM and OPTM. **43**

Figure 26. Performance of global threshold segmentation technique on A549 cancer cell line. (A) and (C) show the segmentation of cytoplasm on central slice of two different A549 cancer cells. (B) and (D) show the segmentation of both cytoplasm and nucleus on central slice of the same cancer cells. **45**

Figure 27. Comparison of coefficient of variations of TEN between OPTM and FCM. **46**

Fig 28. 3D axial views of (A). CacO2 cell (human colorectal adenocarcinoma), (B). HepG2 cell (human liver carcinoma), (C). HT29 cell (human colorectal adenocarcinoma), (D). PC3 cell (human prostate carcinoma), (E). SKBR3 cell (human breast adenocarcinoma) and (F). BT474 cell (human breast carcinoma) stained with Feulgen stain. **48**

Figure 29. 3D images of (A). axial, (B). sagittal and (C). coronal views of an A549 cell (human lung adenocarcinoma) in comparison with 3D images of (D). axial, (E). sagittal and (F). coronal views of NL 20 (normal human lung epithelial cell) stained with Feulgen stain. The nuclear morphology of a cancer cell is distinguishable from a normal cell from culture. NL20 has dense concentrated chromatin content while A549 has a much more complex and heterogeneous chromatin content. **49**

Figure 30. Performance of three different 3D segmentation algorithms used on cancer cells. The left most column shows central slice of the cancer cell followed by segmentation of that cancer cell using gradient method, followed by segmentation of that cancer cell using graph cuts methods, followed by segmentation of that cancer cell using graph cut with convex hull algorithm and finally 3D visualization of cancer cells using graph cut and convex hull to the far right. **54**

List of Tables

Table 1: Results of a right tail F test (followed by Bonferroni correction in p value) between different stains. **32**

Table 2. DNA indices of seven cancer cell lines from OPTM and FCM. **44**

Table 3. Table representing SPF values of different cancer cell lines. **47**

List of Abbreviations

NCI	National Cancer Institute
DCIS	Dental carcinoma in-situ
IDLE	Indolent lesion of epithelial origin
CT	Computed Tomography
FISH	Fluorescence ins-situ hybridization
CCD	Charged couple device
NA	Numerical aperture
DI	DNA index
SPF	S-phase fraction
PI	Proliferation index
DAPI	4',6-diamidino-2-phenylindole
IOD	Integrated optical density value
ACIS	Automated computer imaging system
OPTM	Optical projection tomographic microscopy
FACscan	Fluorescence activated cell sorting scan
CEN	Chicken erythrocyte nuclei
TEN	Trout erythrocyte nuclei
TTEN	Triploid trout erythrocyte nuclei
MSE	Mean square error
FCM	Flow cytometry
ICM	Image cytometry
CV	Coefficient of variation
3D	Three dimension
2D	Two dimension
OCT	Optical coherence tomography

PAT Photoacoustic tomography

ESACP European Society for Analytical Cellular Pathology

Chapter 1: Background and Significance

1.1 What is Cancer?

According to the old definition, cancer is a broad group of diseases in which cells divide and grow uncontrollably, forming malignant tumors and can metastasize to other parts of the body. However there are some premalignant conditions like ductal carcinoma in situ (DCIS) affecting the breast, which satisfies the above definition but is not cancerous (1).

Recently there has been a huge debate where the national cancer institute (NCI) was suggesting whether or not they should redefine cancer. They said that low-risk growths in the breast, prostate and elsewhere should no longer be identified as cancer, and screening efforts to spot

them should be reduced. Renaming of such conditions should be considered relieving stress and fear on patients and also helping them avoid unneeded and potentially harmful solutions.

The advent of highly sensitive screening technology in recent years has increased the likelihood of finding incidentalomas, incidental findings detected during medical scans that most likely would never cause a problem. However, once doctors and patients are aware a lesion exists, they typically feel compelled for biopsy, treatment and removal of the lesion, often at physical and psychological risk to the patient. This issue is often referred to as over-diagnosis, and the resulting unnecessary procedures to which patients are subjected are classed as overtreatment.

The NCI suggested that any lesion detected during lung, breast, prostate and other cancer screening should not be called cancer at all, and should be classified as an indolent lesion of epithelial origin (IDLE) (2).

Hence the modified definition of cancer is a group of diseases in which there is unregulated cell growth, which metastasize to other parts of the body and can be of serious consequences if untreated.

1.2 Current techniques for cancer diagnosis

Currently 30.4 million deaths occur every year from non-communicable diseases. 7.6 million deaths of out these are caused from cancer. 2.5 million deaths could be avoided with early diagnosis, prevention and treatment (3).

Presently, cancer is diagnosed through appearances of signs or symptoms or through screening. People with suspected cancer are investigated with medical test. These commonly are blood test, X-rays, computed tomography (CT) and endoscopy. However neither of these lead to definite

diagnosis. A pathologist makes the final diagnosis after examining the tissue biopsies taken from the suspected organ. They view the biopsies under a bright field microscope and look for special features or characteristic, which distinguishes cancer cells from normal cells (4). Some of which are irregular nuclear membrane, heterogeneous chromatin content, high nucleus to cytoplasmic ratio, macronucleus etc (4,5). They sometimes also search for specific biomarkers using immunohistochemistry techniques such as fluorescent in situ hybridization (FISH) to make definite diagnosis.

1.3 Aneuploidy, a biomarker for cancer diagnosis

Cancer cells generally have an abnormal DNA content with respect to normal cells. This condition is usually referred to as aneuploidy. Aneuploidy is a biomarker, which has been studied extensively in the past for early diagnosis of cancer (6-14). It has also been shown that chromosomal aneuploidy is an early key event in tumour genesis caused by genetic instability (14). Hence an accurate detection of the DNA content of a cell is very important for early diagnosis of cancer.

Because DNA image cytometry results in nuclear integrated optical density (IOD) values in arbitrary units, equivalent but not identical with nuclear DNA content, the quantitation of nuclear DNA requires a rescaling of IOD values by comparison with those from cells with known DNA content, so-called reference cells. DNA content of a cell is generally measured in terms of DNA index (D.I). DNA index is defined as the ratio of the mean DNA content of the G_o/G_1 sample peak divided by the mean DNA content of normal diploid G_o/G_1 human cell peak. Hence there are no units for DNA index as it compares the DNA content of cell relative to a normal human cell.

Similar to DNA index, S-phase fraction (SPF) has also been found to be of prognostic value for cancer diagnosis (15-17). SPF is a measure of cell proliferation and is defined as the percentage of cells in S-phase divided by the percentage of cells in rest of the phases of the cell cycle (Figure 1). The SPF may be used with the proliferative index (PI) to give a more complete understanding of how fast a tumor is growing (18, 19). And the combination of D.I and SPF provides a better classification for prognosis than either one alone. (15, 20-22).

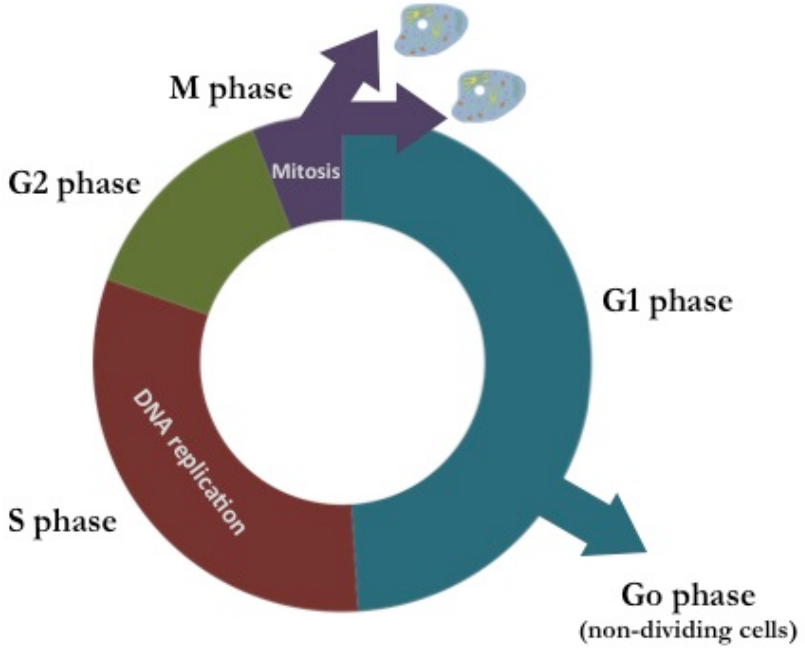

Fig 1. Cell cycle of a cancer cell

1.4 Current techniques for aneuploidy measurement

Currently the two most common techniques to measure aneuploidy are flow cytometry (FCM) and 2D image cytometry (ICM).

1.4.1 Flow cytometry

Flow cytometry is a technology that uses a laser to interrogate a cell flowing past in a stream of liquid. The sample is generally stained with a DNA specific fluorophore (Propidium Iodide or DAPI). As each cell from the sample passes through the laser beam, a series of simultaneous measurements are made and the data is recorded. Three primary measurements are made: forward light scatter (usually representative of cell size); side light scatter orthogonal to the beam (mostly related to cell refractivity or granularity); and finally a series of spectral measurements of fluorescence emission.

FCM is rapid with high throughput and uses fluorescence to quantify the DNA content inside a cell. Hence it is currently considered the gold standard for stoichiometric aneuploidy measurement. However it has few disadvantages like, it does not provide any visual morphological distinction between a cancer cell and a normal cell, which is very important for pathologist for making diagnosis. It requires a large sample, which is often difficult to obtain during biopsies of organs, which are situated deep inside the gastrointestinal tract. Further, though they provide accurate DNA ploidy analysis for near diploid tumors, they cannot distinguish higher aneuploidy in single cells as FCM measures aneuploidy of an entire population of cells. Thus small tumors having high DNA content can be masked by the presence of non-tumor, inflammatory or normal diploid population (23-25). Figure 2 shows a standard flow cytometer from Becton Dickinson.

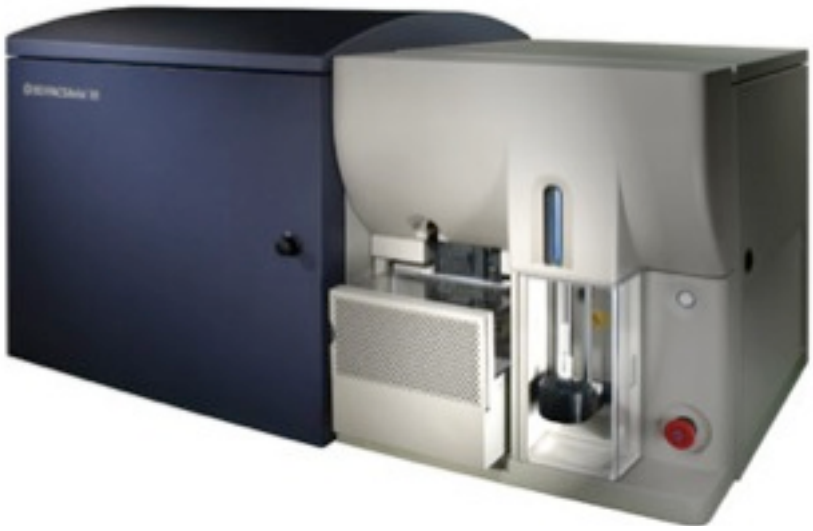

Figure 2. FACSAria™ III from Becton Dickinson

1.4.2 2D image cytometry

On the other hand 2D image cytometer (ICM) is a technology in which the sample is stained with a stoichiometric dye, which could be an absorptive stain or a fluorescent stain. However, the standard technique for quantitative DNA ploidy analysis uses an absorptive stain (usually Feulgen), which binds to the DNA stoichiometrically. After staining the sample on a microscopic slide, 2D optical transmission images are acquired using a bright field microscope (6, 13, 23, 26). Image acquisition is followed by image processing, in which individual cells are segmented using 2D segmentation techniques. Once the cells are segmented, information about the cell and the sample is then derived.

For DNA ploidy analysis, IOD is calculated from intensities of individual cells, which correlates to the DNA content of the cell if the stain is stoichiometric. This whole process

is generally automated and instruments performing them are called automated cellular imaging systems (ACIS). Figure 3 shows a diagram of such an automated cell imaging systems.

Fig 3. EVOS® FL auto cell-imaging system from Invitrogen

ICM is ideal for small size populations. It also provides visual morphological distinction between a cancer cell and a normal cell. Since it looks at individual cells, ICM can identify occasional abnormal cells in the sample. However, one of the major drawbacks of ICM is that it has a low throughput (23, 24). It has the capability to analyze 50 cells/sec as compared to an FCM, which can analyze 5000 cells/sec (27). In ICM, despite the wide acceptance of Feulgen staining there are several disadvantages such as the protocol is complicated and time consuming (28-30). Further, once the sample is stained with Feulgen stain, restaining with other stains is not feasible, which is often required by cytopathologists for additional characterization. Also finding every rare cell and segmenting it out in ICM is very difficult due to overlap and fragmentation (6).

Finally, only 2D images are used for analysis, which give inappropriate results as the cells and their nuclear chromatin features are all 3D. Hence, an analysis using Feulgen stain on traditional ICM may not be the best approach to give accurate results for early cancer diagnosis.

1.5 Research objective

The overall goal of this study is to develop a combined procedure of sample preparation, OPTM imaging and computational processing for stoichiometric aneuploidy measurement.

Since OPTM provides 3D information of single cells, our objective was to use this technology for stoichiometric DNA ploidy analysis. Further, due to the drawbacks of feulgen stain, we investigated other nuclear stains, which binds to the nuclear DNA stoichiometrically and also preserves nuclear morphology. For this, we had chosen acidic thionin stain, which is stoichiometric as well as preserves nuclear morphology in 2D (28, 31-33). We stoichiometrically optimized it for accurate DNA ploidy analysis in 3D. We further compared our results with other common stains used in 2D cytology like hematoxylin (most common stain used in cytology for diagnosis), feulgen (gold standard for stoichiometric aneuploidy measurement) and sytox green (nuclear fluorescent stain).

Chapter 2: Existing 3D Microscopes

Recently, techniques for obtaining 3D information about biological samples have been developed (34-39). However, all are limited to either analyzing tissue samples or analyzing confocal images using fluorescent dyes, making it unsuitable for current needs of cytopathologists who rely on absorption based stains (40). Based on over 100 years of absorption imaging correlation with clinical outcomes, cytopathologists have built a knowledge base for disease diagnosis. Hence, a need for isotropic, high resolution, quantitative 3D imaging using absorption staining is significant. Apart from OPTM there are many other 3D imaging modalities in the market, which could have been used for aneuploidy measurement, however they generally

had few disadvantages over OPTM for this particular application.

2.1 Optical Coherence Tomography

Optical coherence tomography (OCT) is a new type of optical imaging modality analogues to ultrasound imaging, except that is uses light instead of sound. It is based on low coherence interferometry and performs 3D imaging of tissue samples in real time. OCT performs high resolution, cross-sectional tomographic imaging of the internal microstructure in materials and biologic systems by measuring backscattered or backreflected light (38). The images are two-dimensional data sets, which represent the optical backscattering in a cross-sectional plane through the tissue. Although imaging depths are not as deep as with ultrasound, the resolution of OCT is more than 10 to 100 times finer than standard clinical ultrasound. Using OCT in combination with catheters and endoscopes enables high-resolution intraluminal imaging of organ systems.

As compared to OPTM, though OCT is used for tissue morphology, it is still yet to optimized for nuclear morphology. Further it provides low resolution as compared to OPTM and uses scattering as a means for contrast rather than absorption.

2.2 Photoacoustic Tomography

Photoacoustic tomography (PAT) is a 3D imaging technique based on the photoacoustic effect, a phenomena first described by Alexander Graham Bell over one hundred years ago (39). PAT aims to use the advantages of both optical and ultrasound imaging, without their disadvantages. It combines the high contrast from absorption of light with the high resolution and penetration

depth of ultrasound imaging. Hence it is sometimes also referred to as optoacoustic tomography (41).

Basic idea of the photoacoustic effect is simple. Light is shone onto a sample, which absorbs a fraction of the incident energy. This energy is converted into heat. The temperature rise leads to thermoelastic expansion of the object. This sudden pressure rise propagates as a sound wave, which can be detected. By detecting the pressure waves, one can localize their source (i.e., where light was absorbed) and obtain important information about the studied sample. Real-time 3D photoacoustic imaging has the potential to capture the physiology and pathology associated with dynamic phenomena in three-dimensional space. Within the last decade, the photoacoustic effect has been successfully used for *in vivo* biomedical imaging of different biological tissues.

As compared to OPTM, again PAT is generally used for analysing tissue morphology and is still yet to be optimized for nuclear morphology. Further though it uses absorption as a means for contrasts, it is extremely slow as compared to OPTM. Hence, the time it would take to analyze a sample would be high.

2.3 Confocal Microscopy

Confocal microscopy is another imaging modality that provides high-resolution 3D images of specimens. The basic idea of confocal fluorescence microscopy is that it actively suppresses any signals coming from out-of-focal planes. Confocal microscope uses point source illumination and a pinhole in an optically conjugate plane in front of the detector to eliminate out-of-focus signals. As only light produced by fluorescence very close to the focal plane can be detected, the image's optical resolution, particularly in the sample depth direction, is much better than that of the traditional wide-field optical microscopes (42). However, as much of the light from sample

fluorescence is blocked at the pinhole, this increased resolution is at the cost of decreased signal intensity. In the biomedical sciences, a major application of confocal microscopy involves imaging either fixed or living cells and tissues that have usually been labeled with one or more fluorescent probes.

As compared to OPTM, confocal microscopes generally use fluorescence as a means for contrast. Though some use absorption, but they are not commercially yet available. They generally use lasers instead of halogen lamp, which makes them extremely expensive for use. Further confocal microscopy does not provide isometric resolution like OPTM, which is very important for 3D reconstruction. As a result, confocal microscopes maybe perfect for 3D viewing of specimens, but not for performing quantitative studies.

Chapter 3: Optical Projection Tomographic Microscopy

3.1 Introduction

3D optical projection tomographic microscopy (OPTM) combines attributes of both computed tomography (CT) imaging with slow-flow cytometry. Unlike FCM or ICM, OPTM provides 3D morphometric data like volume, shape and nuclear texture, which is very important for cytopathologists who primarily rely on morphology of cell for cancer diagnosis. Thus it provides quantitative cytometry along with 3D visualization of morphology.

OPTM images single cells and proving 3D information about them. Figure 4 shows a basic setup of an OPTM. It has also been shown in a study that as compared to 2D images, OPTM-captured 3D images of single cells result in threefold reduction in false negative rates for adenocarcinoma detection without affecting its high specificity of 96% (43) (Figure 5).

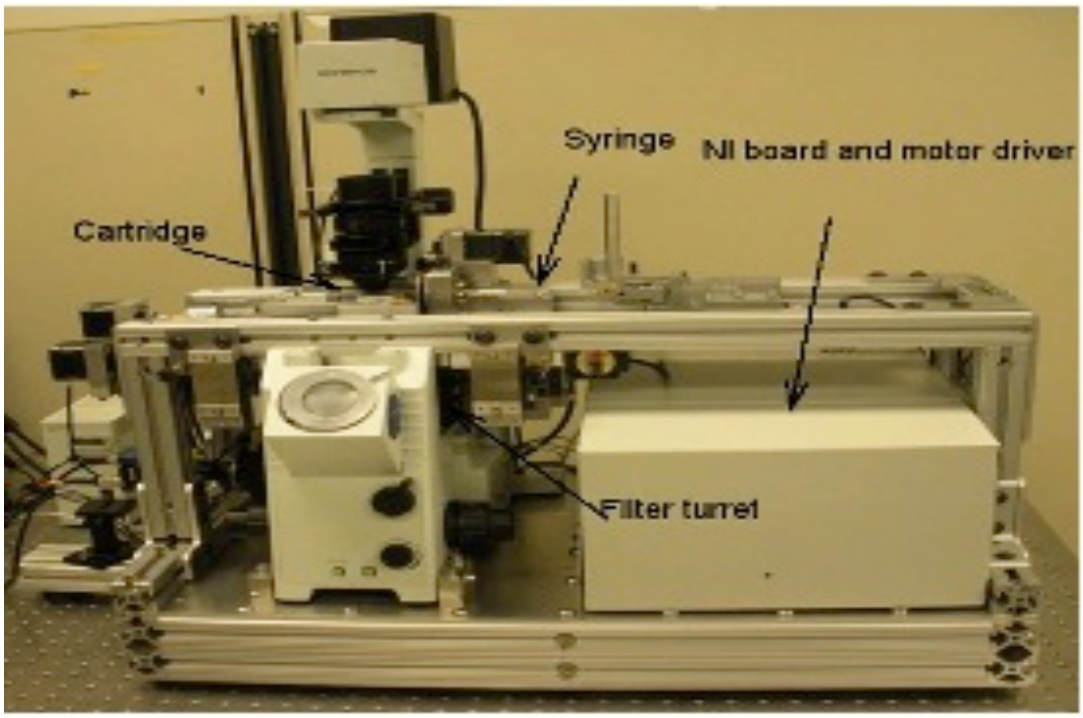

Fig 4. Basic setup of an optical projection tomographic microscopy (OPTM)

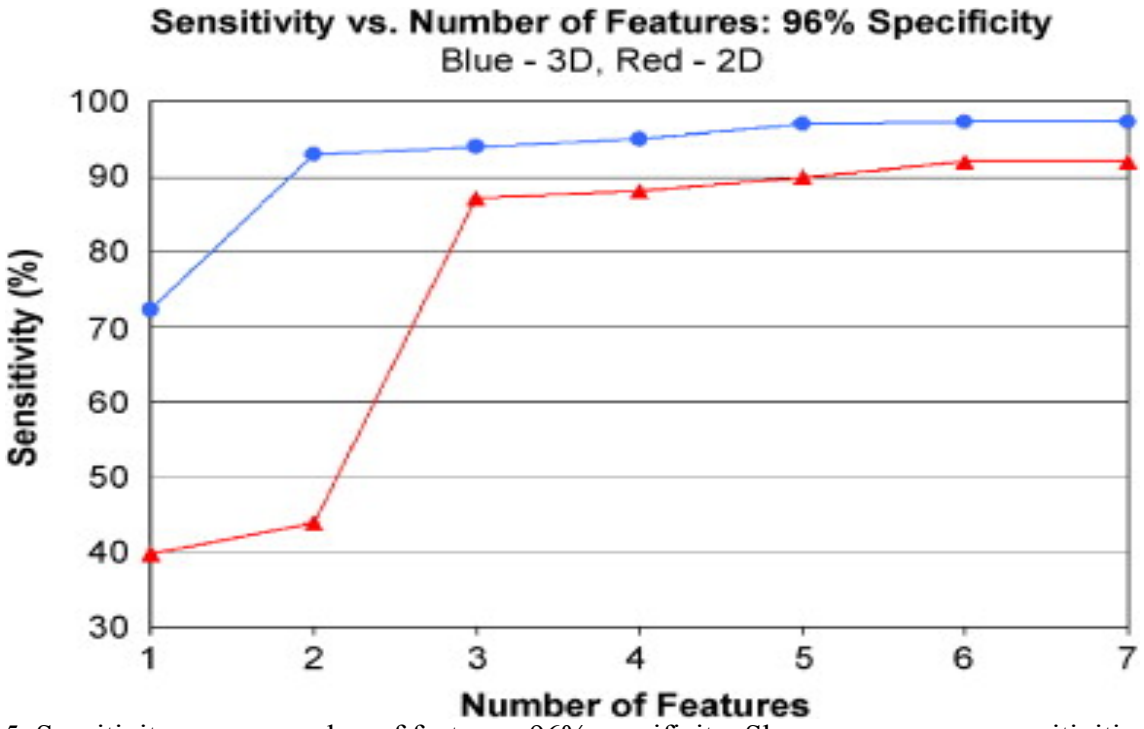

Fig 5. Sensitivity versus number of features: 96% specificity. Shown are average sensitivities for 3D (blue) and 2D (red).

OPTM generates 3D, submicron, isometric and high-resolution images of nuclear features (44). In addition, OPTM can perform multimodal imaging (45) generating both bright field transmission image as well as a fluorescence image with exact co-registration.

In the present study, we used OPTM along with an automated method for 3D nuclear segmentation to compute the DNA content on a cell-to-cell basis using different absorption and fluorescent stains for early cancer diagnosis. Since the entire volume of the nucleus is measured, there is less uncertainty in the measure of total DNA content as every voxel is used to calculate the integrated optical density. Variations in perspective of the nucleus from 2D images are eliminated in a single OPTM image. Hence, quantitative 3D imaging on single cells using OPTM is expected to provide more accurate and robust results as compared to a traditional ICM.

3.2 Construction

The system was built on a wide-field optical microscope (Olympus IX71) with custom-designed microcapillary-based rotation stage (44). Since OPTM can do multimodal imaging, both absorption as well as fluorescence imaging was performed on the same instrument (45). For absorption imaging, the light from the halogen lamp (QTH) is filtered by a diffuser and a color filter. The filters were chosen so as to match the spectral properties of the absorptive dyes, 585±60 nm and 546±20 nm for thionin/hematoxylin and Feulgen staining respectively (46, 47). From the filter light passes through a 0.9 numerical aperture (NA) condenser, which focuses the light onto the sample, collected by the objective lens and sensed by the monochromatic charged coupled device (CCD) camera (Prosilica GE1650, 1600x1200, 7.4μm pixel size). On the other hand for fluorescence imaging, an epi-fluorescence setup was used, in which light from the LEDs (pE100, Cool LED, UK) was filtered by an excitation filter and then reflected to an objective lens by a dichromic mirror. Fluorescence signals from the sample were collected by the objective lens, passed through the dichromic mirror, and were then filtered by an emission filter before reaching the camera. Spectral properties of the fluorescent dye were matched with both the excitation and the emission filter. Figure 6 shows a schematic diagram of an OPTM.

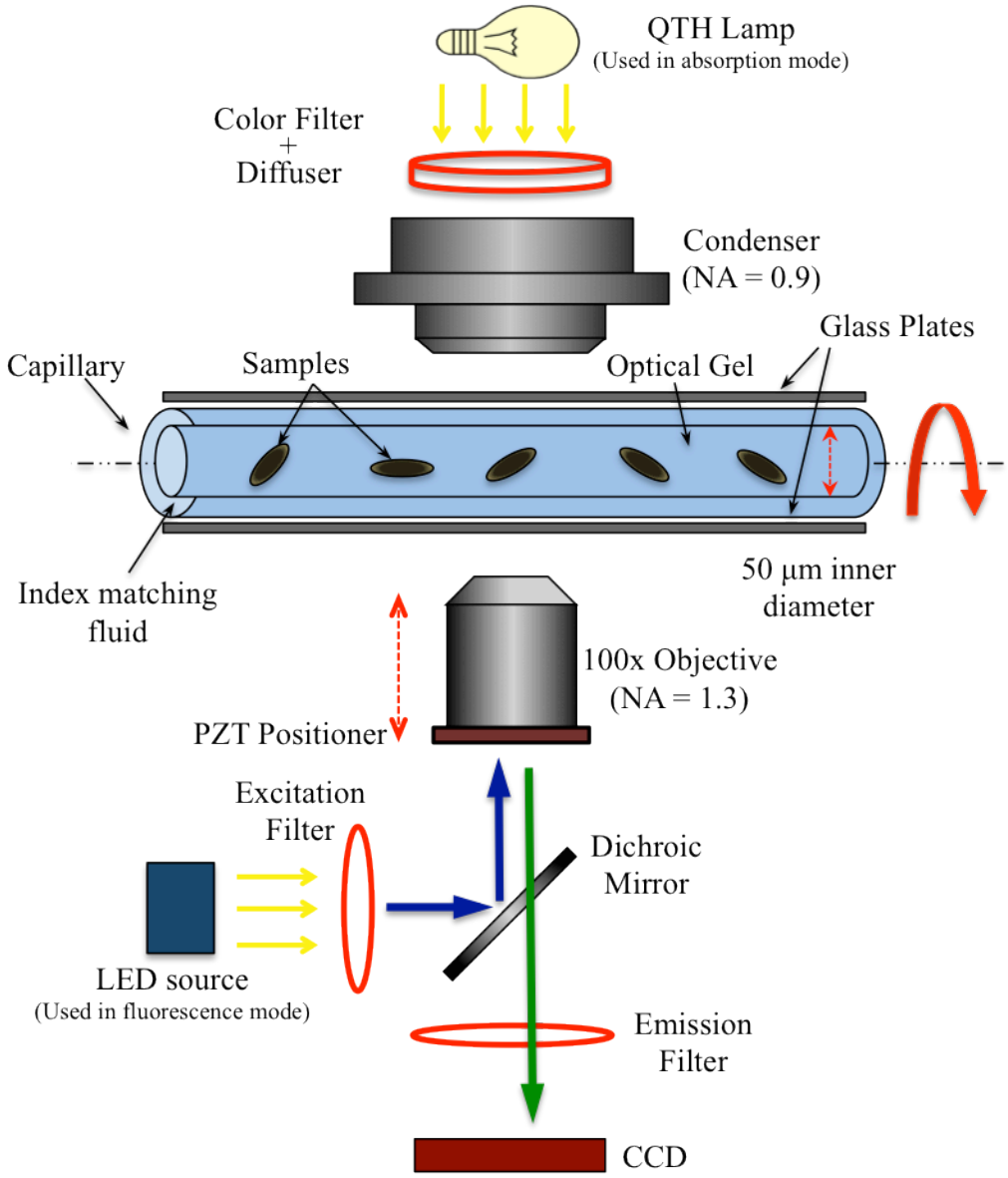

Fig 6. Schematic diagram on an OPTM

The sample is flowed through a 50-micron inner diameter capillary tube. The tube rotates in an oil-filled space between two flat, parallel glass slides. The optical gel (Nye SmartGel OC431A-LVP) in which the sample is immersed and the oil, maintains a constant refractive index both inside and outside the capillary, thereby minimizing the optical distortion caused by the

curvature of the tube.

3.3 Image acquisition

Images are acquired using a process similar to that of a normal X-ray CT scan. A pseudoprojection image is taken by axially scanning the objective focal plane through the sample and optically integrating all the focal plane images using a high numerical aperture objective (NA 1.3, 100x oil). The objective is mounted on a piezoelectric (PZT) positioner (NV40/1CL, Piezosystem Jena, Jena, Germany), which is focused to the CCD camera. The axial scanning range is adjusted for different samples in order to cover the entire sample. 500 such pseudoprojection images are taken in one complete rotation by rotating the capillary tube at uniform angular intervals of 0.72 degrees. The specimen location inside the tube is also tracked, so that accurate focal plane scanning could be accomplished during tube rotation.

3.4 Image reconstruction

The 500 2D pseudoprojections obtained during image acquisition are then reconstructed using filtered backprojection algorithm (similar to what is being used in X-ray CT) to obtain the 3D structure of the specimen.

3.5 3D Segmentation

3D segmentation of the reconstructed images is done at Cornell University (Ithaca, NY). Image segmentation for the nucleus and the cytoplasmic regions in 3D optical microscope images is based on the observation that three primary regions (background, cytoplasm and nucleus) have significantly different image intensities. Hence the nucleus has the highest image intensity followed by the cytoplasm and finally the background. The automated 3D segmentation technique uses a global threshold based on image intensity gradients.

Single cell segmentation method is based on two observations. First, manual markings are well matched to an image threshold (as is the case for x-ray based CT images as the reconstruction image intensity is directly related to the optical density) as shown in Figure 7. Second, there is a high image gradient in most of the transition region between the two different primary regions. However the gradient is not uniform along the border of the targeted region so it cannot be used as the only information for region segmentation. From empirical tests it was found out that the maximum in the laplacian is best correlated with the manual markings of boundary of different region types.

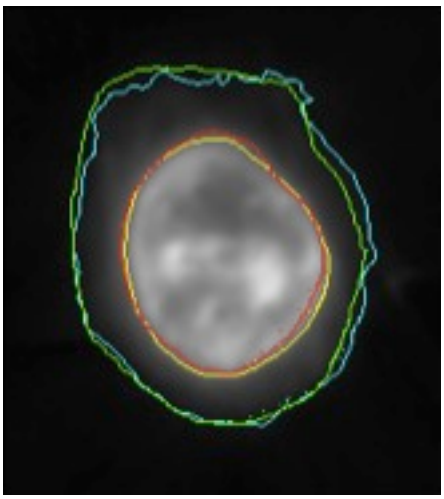

Fig 7. Central slice of a cell showing agreement of manual markings (cyan and yellow) with that obtained from computer using image threshold (green and red).

For a cell, first such transition occurs at the surface boundary of the cytoplasm and the background and for nuclei, it occurs at the surface of the nuclear envelope. For an optical-tomography 3D image I, with a central image slice I_c, the following were the steps used for 3D segmentation of the nuclei from the background (or cytoplasm in case of a cell):

1. Edge enhancement was carried out using an algorithm from Deriche (48, 49). The gradient magnitude of the central slice image I_c was calculated. Further, its gradient magnitude was computed and termed as g_c.

$$g_C = \left\| \nabla \| \nabla (I_C) \| \right\|$$

2. A merit mapping of I_c was generated, where for every possible image intensity i, a merit value (m_i) was computed. For this, the boundary (B_i) of the binary region selected by that image intensity was computed. After which, the mean value of the gradient image (calculated in step 1) over the pixels belonging to the region boundary was calculated and termed as merit value:

$$m_i = \left(\sum_{B_i} g_c \right) / \| B_i \|$$

3. The peaks in the merit map serve as the threshold to segment the three primary regions. Typically for a cell, the threshold that corresponds to the first peak (maximum value) of the merit mapping (i.e. the mean gradient) is selected as the segmentation threshold for the cytoplasm and the threshold that corresponds to the second peak is selected as the segmentation threshold for the nucleus. For the nuclei, since they don't have cytoplasm, only the first peak was considered to compute the full 3D segmentation of the nuclear region.

As an example, Figure 8 and Figure 9 shows image analysis on an A549 (human lung adenocarcinoma) stained with feulgen and triploid trout erythrocyte nuclei (TTEN) stained with 45 minutes thionin stain respectively.

In both examples there were two significant peaks in the merit function graph. In case of an A549, the first peak correlated to the cell boundary, which separates the cytoplasm from the background. And the second peak correlated to the nuclear boundary, which was used for computing the IOD. On the other hand for the TTEN nuclei, only the first peak was used as an estimate to compute the threshold for the nuclear membrane, though there was no visible feature in the histogram relating to that value. The second peak corresponds to features within the nucleus. Surface rendering of the whole segmented region for both the cell and the nuclei are also shown for three orthogonal viewing directions (Figure 8. E-G and Figure 9. E-G). The blue colour in Figure 8 represents the cytoplasm while the yellow represents the nucleus. In Figure 9, the blue colour represents the residual staining of the 45min thionin stain, while yellow again represents the nucleus.

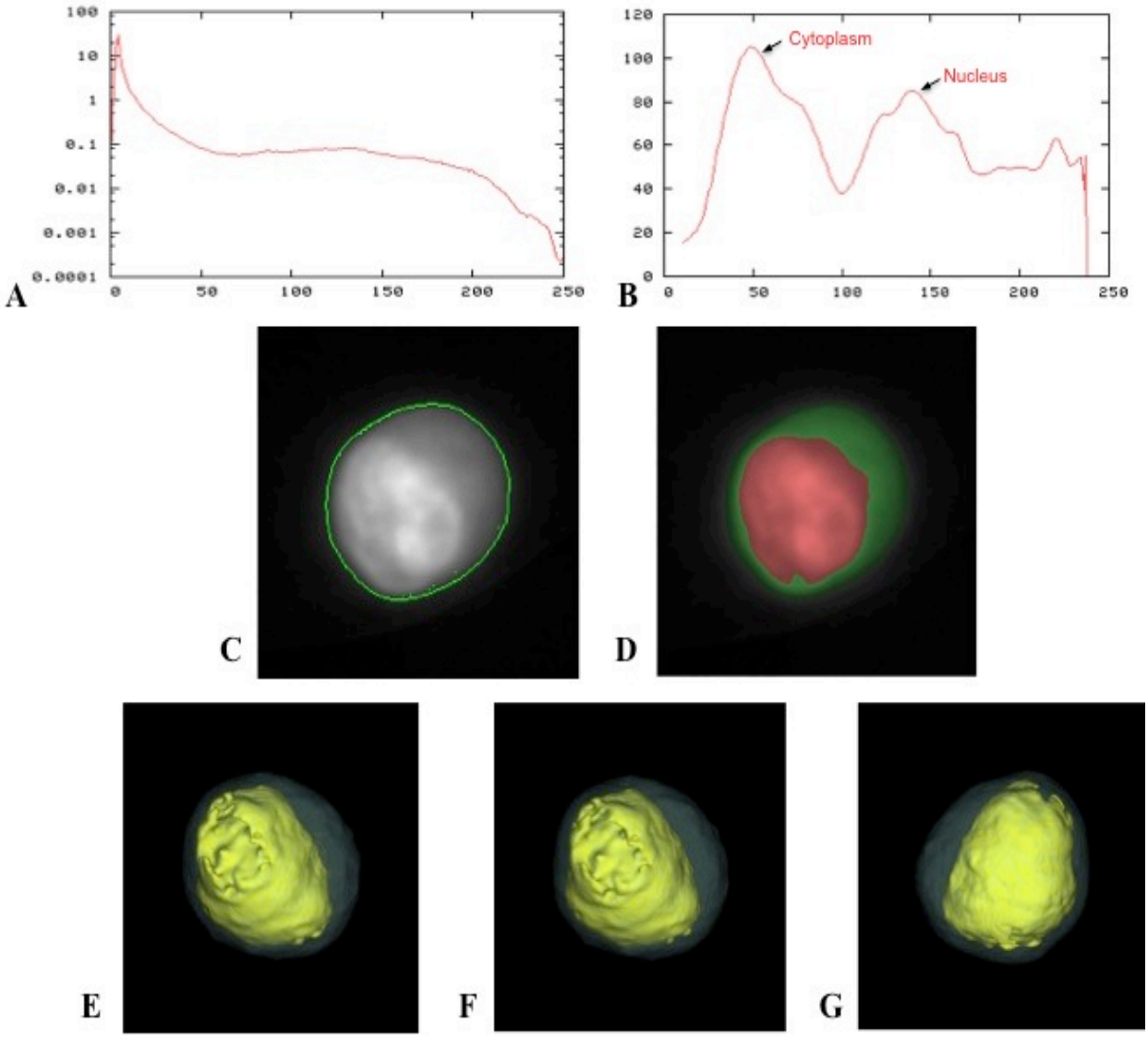

Fig 8. 3D segmentation of an A549 stained with feulgen stain. (A). Histogram and (B). Merit function (m_i) of the central slice (I_c) of the image across the same range of intensity values. (C). Central slice of A549 cell with first peak used as the threshold (D). Central slice of A549 cell with both the peaks used as the threshold. 3D surface rendering of (E). axial, (F). sagittal and (G). coronal views of A549 cell computed by applying automatically determined thresholds to the whole 3D image.

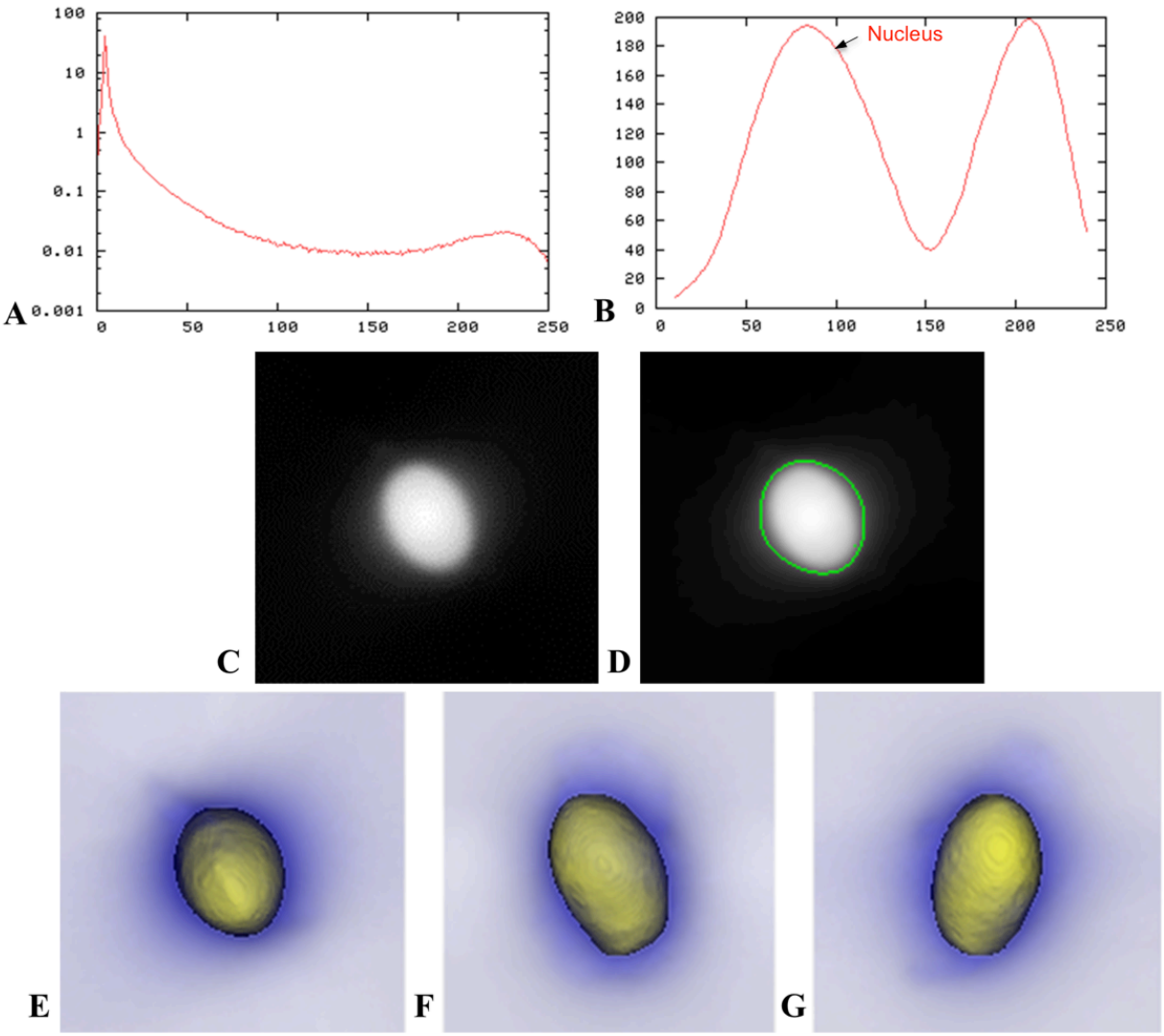

Fig 9. 3D segmentation of TTEN stained with 45min acidic thionin stain. (A). Histogram and (B). Merit function (m_i) of the central slice (I_c) of the nuclei image across the same range of intensity values. (C). Central slice of TTEN nucleus image (D). Central slice of TTEN nuclear region with the first peaks used as the threshold. 3D surface rendering of (E). axial, (F). sagittal and (G). coronal views of TTEN nuclear region computed by applying automatically determined threshold to the whole 3D image.

Chapter 4: Calibrating OPTM for stoichiometry DNA ploidy analysis

4.1 Sample Preparation

Chicken erythrocyte nuclei (CEN), Trout erythrocyte nuclei (TEN) and Triploid trout erythrocyte nuclei (TTEN) (Biosure, Inc. USA) were used as internal standards to calibrate the OPTM (Figure 10). Human lymphocytes (HemaCare Corporation, USA) were used to calculate the D.I of each internal standard using FCM.

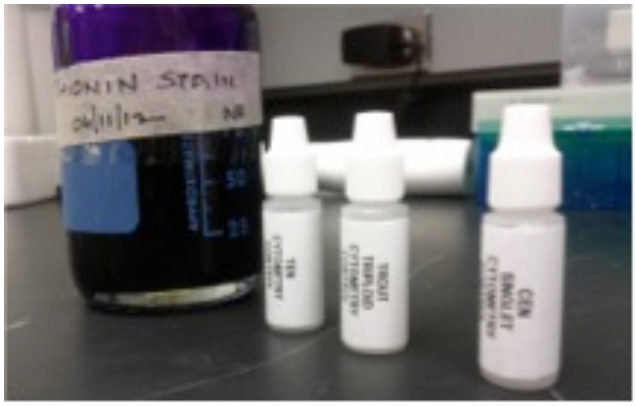

Fig 10. Diagram showing the three internal standards along with acidic thionin stain.

4.2 Flow cytometry

Flow cytometry was performed in Dr Peter Rabinovitch laboratory, Department of Pathology, at University of Washington. Standard FCM was performed on all the three samples and lymphocytes, which were fixed in 50% ethanol according to the conventional protocol and the manufacturer's instruction (50). Each sample was resuspended in an isotonic pH 7.4-buffered solution with 0.1% nonidet P-40 detergent, 10 μg/ml diamidino-2-phenylindole (DAPI) and 1% RNAse, triturated with a 26 gauge needle, and filtered through 40 mm steel mesh. The analysis was performed using an InFlux cytometer (BD Biosciences, USA) with UV excitation. A total of 20,000 cells were analyzed, and in all cases, a coefficient of variation (CV) below 4.0% was found. The DNA index and S-phase fraction (SPF) were analyzed for each internal standard in comparison with lymphocytes using the software program MultiCycle (Phoenix Flow Systems, San Diego, CA, USA) (51).

4.3 3D Image cytometry

Hematoxylin, thionin, Feulgen and sytox green were used on equal volumes of CEN, TEN and TTEN for quantitative analysis of DNA content. Thionin stain was optimized for stoichiometry

by varying the staining time periods. To avoid batch-to-batch variations, thionin stain was prepared in the laboratory while Feulgen, hematoxylin and sytox green were preordered.

4.3.1 Acidic Thionin Staining

We prepared the acidic thionin stain in our laboratory as per protocol from a previously published study (52). 13.3 mL of acetic acid is mixed with 24 gm. of tris® base and added 650 ml of water until the reagents got dissolved with constant stirring. Methanol was then added to make the final volume of 1000 ml. Thereafter, 10 gm. of thionin acetate (Sigma Aldrich, USA) was added followed by continuous stirring for an hour. The solution was then filtered through Gelman filter and a final thionin stain of pH of 6.8 was achieved.

After preparation of the stain, 500μL of each standard was fixed with 50% ethanol and then stained with acidic thionin for 15mins, 30 mins and 45 mins using the suspension technique. In this technique, we took 500 μL of the sample, and centrifuged it at 500g for 5 minutes. We aspirated out the supernatant, leaving behind the sample. To this we added 200 μL of thionin stain and waited for 10 minutes, 25 minutes and 40 minutes before it was centrifuged at 500 g for 5 minutes; hence the total staining time achieved was 15 minutes, 30 minutes and 45 minutes respectively. After that we washed it with gradations of ethanol (50%-100%) and later with xylene twice before inserting it into syringes with optical gel.

4.3.2 Hematoxylin Staining

Similarly for hematoxylin, 500μL of the sample fixed in 50% ethanol was taken and centrifuged at 500g for 5 minutes. We aspirated out the supernatant, leaving behind the sample. To this we added filtered tap water to make the volume 100μL and then added 25 μL of 0.22 μm syringe-

filtered Gill's Hematoxylin solution #1 (Electron microscopy sciences, USA). We centrifuged it immediately at 500g for 5 minutes and later aspirated out the supernatant. The excess stain was washed out with two washes of filtered tap water. Then the sample was dehydrated with gradations of ethanol (50%-100%) and later washed twice with xylene before inserting into the syringe with the optical gel.

4.3.3 Feulgen Staining

The Feulgen staining was performed following a well-established protocol (53-56). 500μL of the sample, which had been fixed with Bohm's fixative, was centrifuged at 500g for 5 minutes and the supernatant was aspirated out leaving behind the sample. This was followed by washing the sample with distilled water and hydrolyzing it using 5M HCl at 22 degree Celsius for 40 minutes. Thereafter excess HCl was washed using distilled water and later the sample was stained with Schiff reagent solution (Fisher Scientific, USA) for 45 min. The sample was then washed with sodium bisulphite solution and distilled water. Later it was dehydrated with gradations of alcohol (50%-100%), washed twice with xylene before inserting it into the syringe with the optical gel.

4.3.4 Sytox Green Staining

Similar protocol, which was used for hematoxylin was followed. Samples, which were fixed in 50% ethanol, were washed with filtered tap water before staining with sytox green solution (1:5000 dilution from stock, Invitrogen, USA) for 10 mins. We centrifuged it at 500g for 5 min and later aspirated out the supernatant. Then the sample was dehydrated with gradations of ethanol (50%-100%) and later washed twice with xylene before inserting into the syringe with the optical gel.

All the syringes are later imaged using the OPTM to obtain 500 pseudo projections and 3D segmentation is then performed on the reconstructed nuclei as previously described.

4.4 DNA content analysis

Using the previously mentioned segmentation algorithm with implementation in the VisionX/SIMBA environment (57), 3D segmentation of the fifty-stained CEN, TEN and TTEN were achieved. Camera sensor was assumed to be linear and uniform illumination was maintained. All samples were fixed, stained, and imaged under constant conditions, to allow a direct comparison of the measured data. For each nucleus, intensities of all the voxels in the segmented nuclear region were added to obtain the total IOD of the 3D nucleus. Since all the four stains are nuclear stains, the IOD of the 3D nucleus should correlate to the total amount of DNA content in that nucleus (Figure 11).

For calibrating the OPTM for stoichiometry, the ratios of DNA indices of the internal standards from our technique were compared to which is FCM. Three ratios TTEN/TEN, TEN/CEN and TTEN/CEN were used for analysis. The ratios of the IOD between the three nuclei for all the stains gave us the corresponding ratios of their DNA indices.

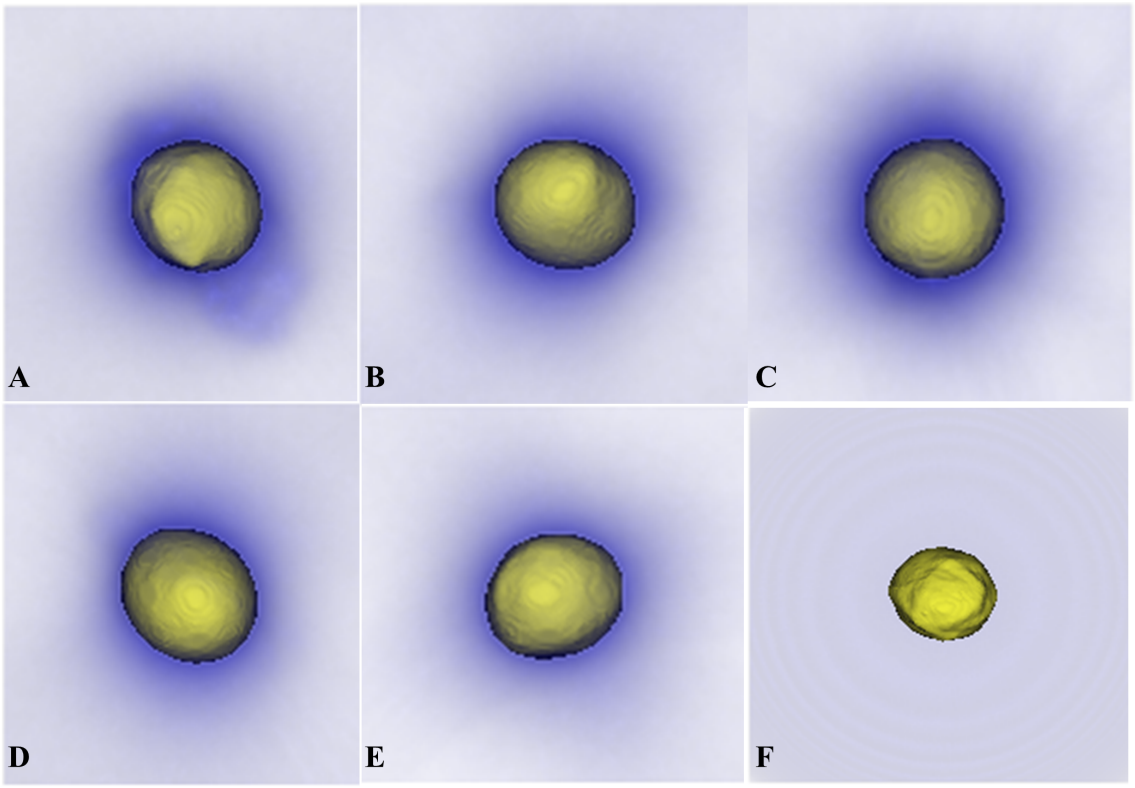

Fig 11. 3D renderings of the axial view of a TEN stained with (A). hematoxylin, (B). 15min thionin, (C). 30min thionin, (D). 45min thionin, (E). Feulgen and (F). sytox green.

4.5 Results and Discussion

All statistical analysis was performed using either Matlab (MathWorks, Version R2012a, Natick, MA, USA) or Stata (StataCorp LP, Version 12.0, College Station, TX, USA). The variances of all the four stains were analyzed using a modified right tail F test after Bonferroni correction (58, 59). For analyzing stoichiometry, the mean square error (MSE) between the ratios of each individual observation and that obtained from FCM was computed for the all the stains.

The mean and the standard deviation of fifty ratios of individual observations for different stains using OPTM along with ratios of DNA indices obtained from FCM are shown in Figure 12. Feulgen was the most stoichiometric stain among hematoxylin and sytox green as shown (Figure

12A). Thionin with 45min of staining time showed best results among different thionin staining times (Figure 12B).

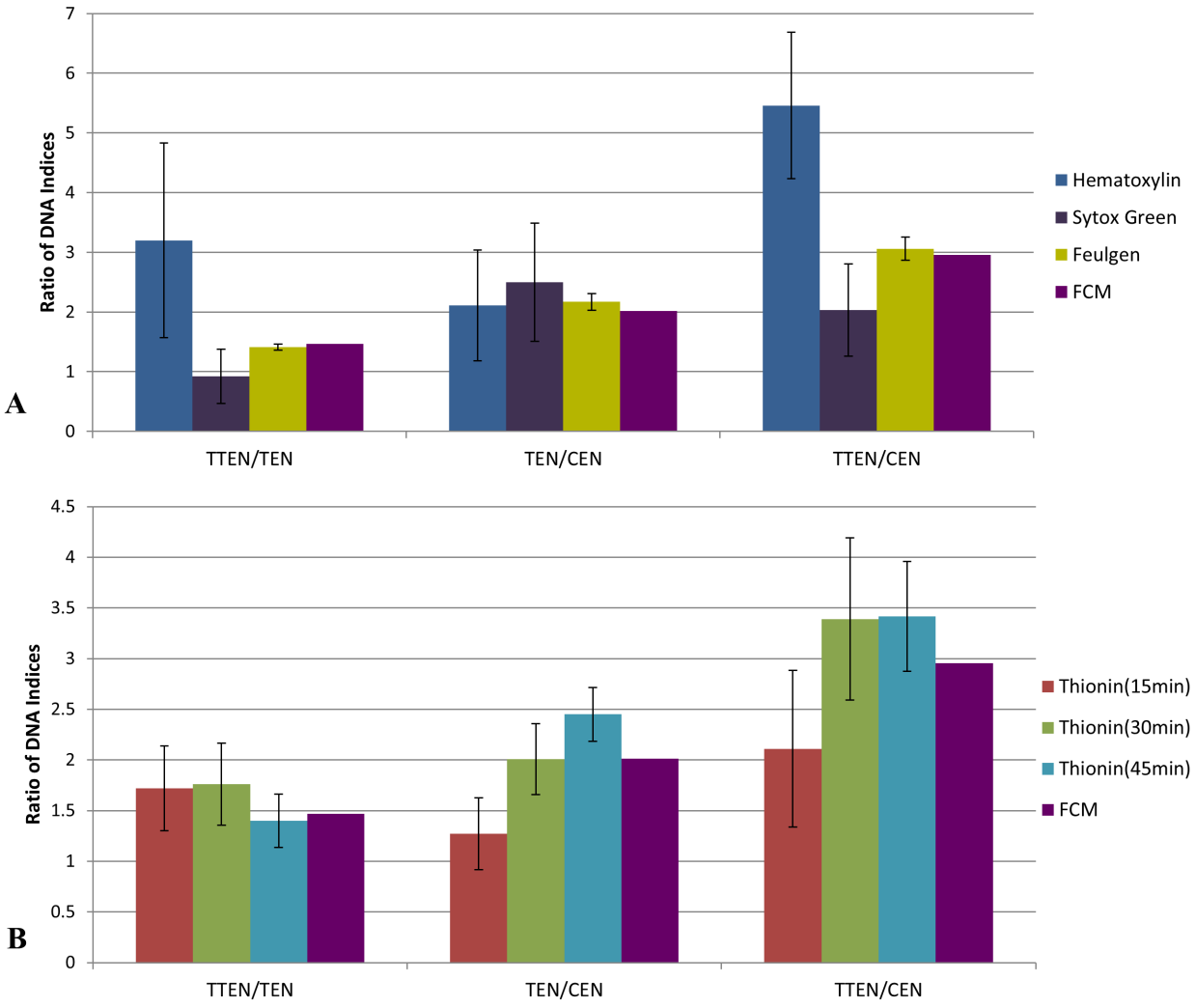

Fig 12. (A). The mean and the standard deviation of 50 ratios of individual observations for hematoxylin, sytox green and Feulgen stain along with ratios of DNA indices obtained from FCM. (B). The mean and the standard deviation of 50 ratios of individual observations for different thionin staining times along with ratios of DNA indices obtained from FCM.

4.5.1 Stoichiometry

The MSE of TTEN/TEN, TEN/CEN and TTEN/CEN were highest with hematoxylin staining and least with Feulgen staining. Among different thionin staining times, 45min thionin had least MSE while 15min thionin had the highest. Sytox green MSE was greater than both thionin and Feulgen staining but less than hematoxylin as shown in Figure 13.

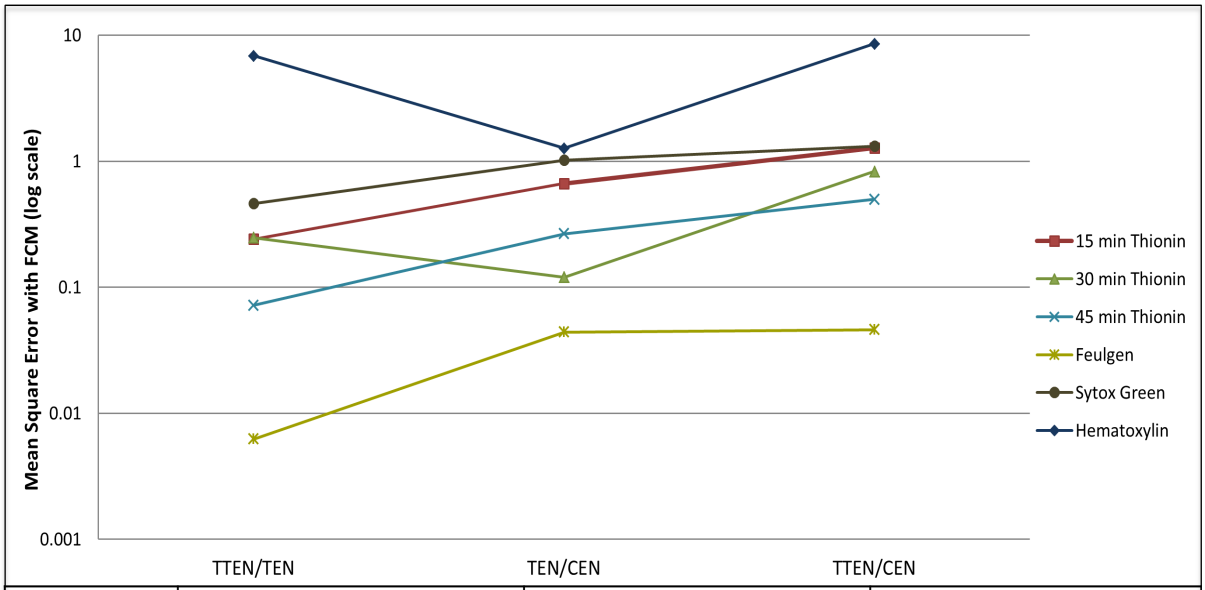

	TTEN/TEN		TEN/CEN		TTEN/CEN	
	Mean ± SD	**95% C.I**	**Mean ± SD**	**95% C.I**	**Mean ± SD**	**95% C.I**
Hematoxylin	6.875±11.707	10.647-3.103	1.266±3.796	2.489-0.043	8.533±11.74	11.840-5.265
15 min Thionin	0.214±0.381	0.122-0.360	0.665±0.384	0.510-0.818	1.275±0.939	0.900-1.651
30 min Thionin	0.247±0.362	0.147-0.347	0.120±0.116	0.086-0.154	0.83±1.29	0.453-1.207
45 min Thionin	0.072±0.242	0.001-0.142	0.265±0.2701	0.186-0.344	0.498±0.945	0.222-0.774
Feulgen	0.006±.0072	0.002-0.009	0.044±0.047	0.22-0.067	0.046±0.065	0.014-0.078
Sytox Green	0.462±0.468	0.051-0.872	1.02±1.61	-0.387-2.430	1.32±0.653	0.753-1.899

Fig 13: The MSE and its standard deviation along with 95% confidence interval of different stains.

The MSE of TEN/CEN in Figure 13 was slightly more for 45min thionin than 30min thionin possibly because male CEN tend to have a higher DNA content than female CEN (60, 61). Both

male and female trout erythrocytes have almost the same size of sex chromosomes and hence the DNA variations due to sex related changes could be ignored for them (61). And since we had used mixed populations of both CEN and TEN, this could have led to an increase in the ratios of DNA indices when CEN is present in the ratios.

4.5.2 Variability

The variance of hematoxylin staining was statistically greater than 45min thionin as well as Feulgen staining for all the three ratios. The variance of 45min thionin was also statistically greater than Feulgen staining for all the three ratios. The variance of sytox green was statistically greater than Feulgen staining but not statistically greater than 45min thionin for all the three ratios as shown in Table 1. The variance of sytox green and hematoxylin were statistically not significant ($p>0.01$) when compared using a two tail paired F test.

	TTEN/TEN	**TEN/CEN**	**TTEN/CEN**
Hematoxylin and 45min Thionin	$p < 0.00005$	$p < 0.00005$	$p < 0.00005$
Hematoxylin and Feulgen	$p < 0.00005$	$p < 0.00005$	$p < 0.00005$
45min Thionin and Feulgen	$p < 0.01$	$p < 0.01$	$p < 0.01$
Sytox Green and Feulgen	$p < 0.005$	$p < 0.005$	$p < 0.005$
Sytox Green and 45min Thionin	$p > 0.01$	$p > 0.01$	$p > 0.01$

Table 1: Results of a right tail F test (followed by Bonferroni correction in p value) between different stains.

4.5.3 Morphology

Morphology was visually compared for all the stains with assistance from Florence W Patten (CT (ASCP), CFIAC), who is an experienced cytotechnician. Morphology was only preserved

for feulgen and hematoxylin stain as shown in Figure 14 and Figure 15 respectively. While, 45min thionin showed good stoichiometry, it did not appear to preserve the morphology Figure 16.

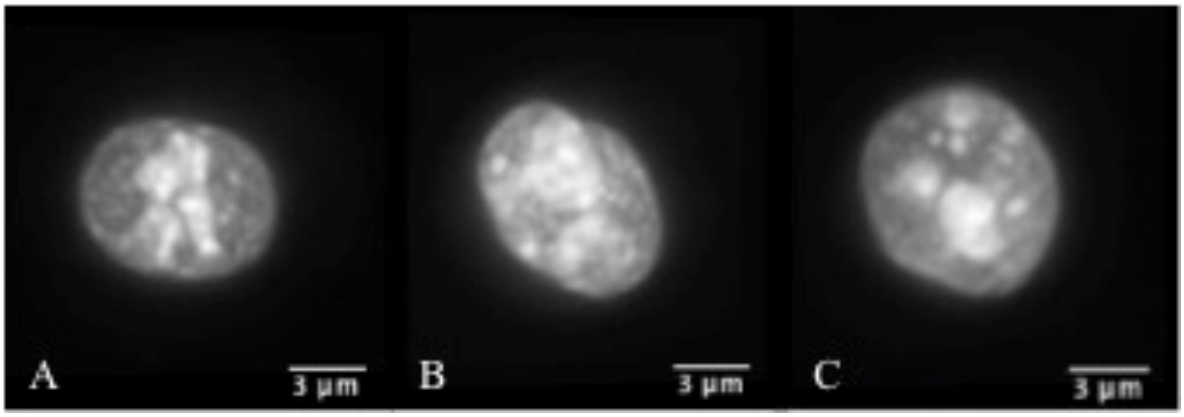

Fig 14. 3D visualization of morphology for three different A549 cancer cells stained with feulgen stain.

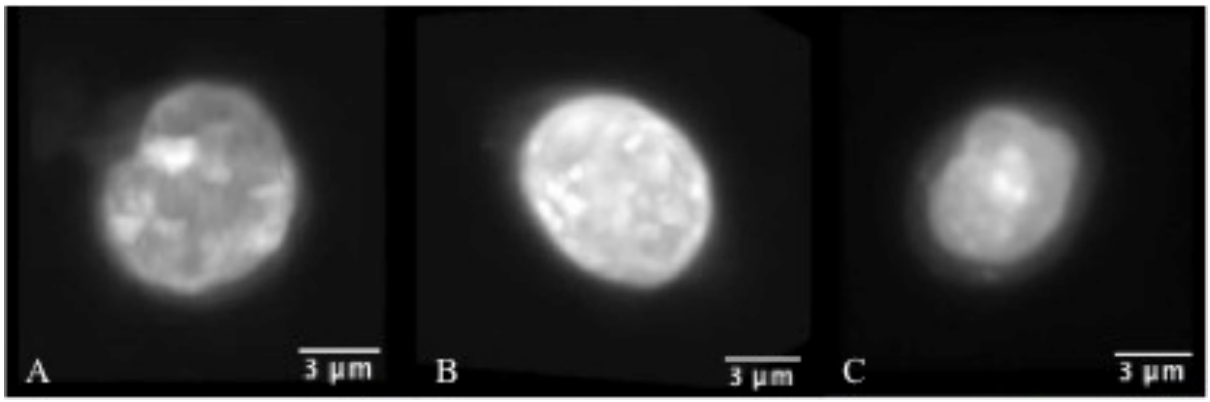

Fig 15. 3D visualization of morphology for three different A549 cancer cells stained with hematoxylin stain.

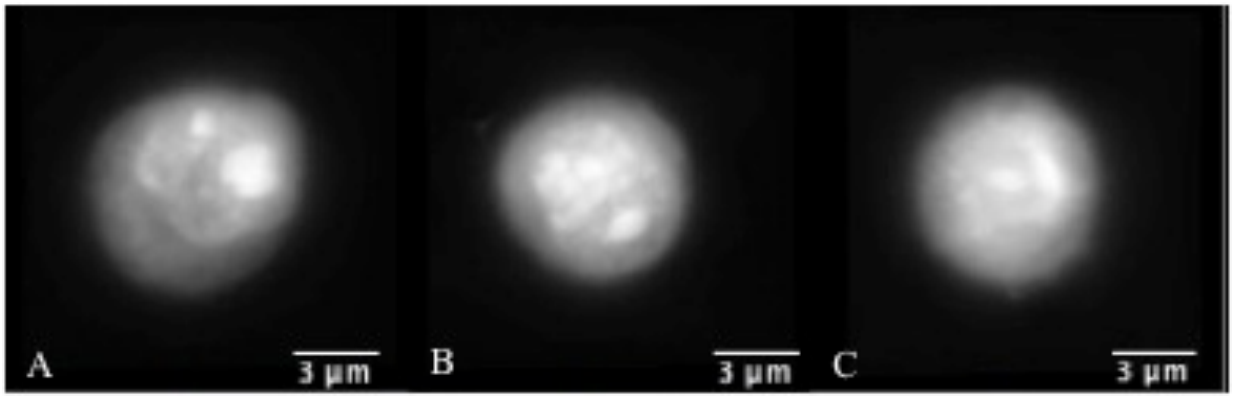

Fig 16. 3D visualization of morphology for three different A549 cancer cells stained with acidic thionin stain having a staining time of 45 minutes

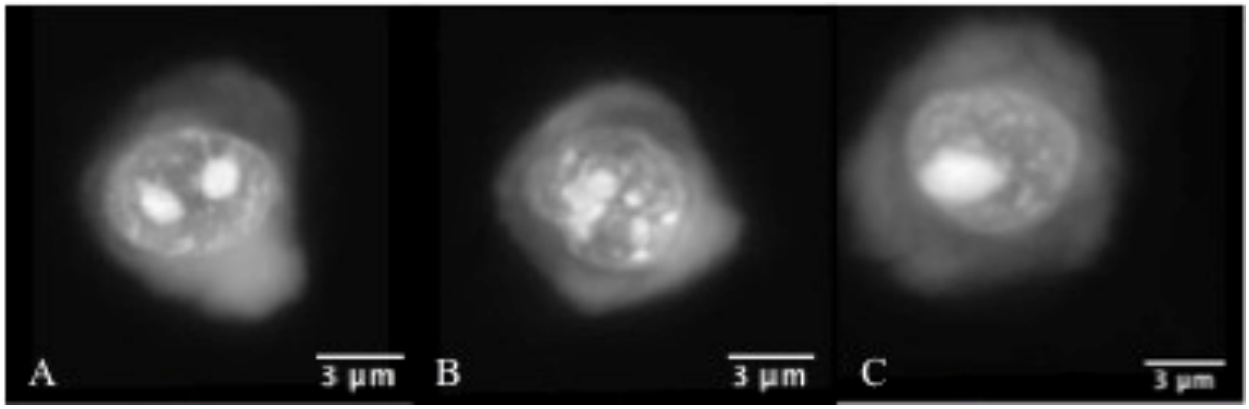

Fig 17. 3D visualization of morphology for three different SKBR3 cancer cells stained with acidic thionin stain having a staining time of 30 seconds.

Figure 17 shows an extreme case in which the morphology of SKBR3 cells (cultured human breast adenocarcinoma) was preserved when stained with 30 seconds of acidic thionin. We have combined some of the benefits of both FCM and ICM, by developing a technique where we can analyze the DNA content of a cell in 3D without appearing to compromise the nuclear morphology of the cell. This required two steps, an initial staining of the cell by a stoichiometric stain followed by 3D imaging of the stained cell. We have demonstrated not only quantitative DNA staining but also the automated measure of nuclear volume from 3D images.

Feulgen stain, the gold standard for stoichiometry in 2D (62-64), showed best results in 3D as determined by highest accuracy (least mean square error) to FCM and least measurement variance. We optimized the staining time of acidic thionin for stoichiometry and have shown that 45 minutes of staining time is the next best stain for stoichiometry. As expected, it outperformed hematoxylin, the most common stain used in cytology (28, 33). However, nuclear morphology did not appear to be preserved for 45min of thionin staining time, making it less suitable for quantitative DNA analysis. Both hematoxylin and Feulgen preserved nuclear morphology and hence Feulgen stain can be considered as the overall gold standard for quantitative DNA analysis in 3D as well.

Like 2D ICM, hematoxylin stain visually enhances nuclear morphology, but showed high variance and least stoichiometricity in 3D. Consequently, after having been used in diagnostic cytology for more than a century, batch-to-batch variation, non- specific binding to the nucleus and cytoplasmic regions makes it inapt for quantitative assessment of DNA (28, 33). On the other hand, Feulgen stain like in 2D is highly stoichiometric, showed the least amount of variance and appeared to preserve nuclear morphology in 3D as well (Figure 14). Sytox green was neither stoichiometric nor preserved nuclear morphology. As shown in Figure 11, residual cytoplasmic staining was observed for all the absorption stains. However, as compared to other absorption stains, it was reduced for Feulgen staining. Sytox green showed no residual cytoplasmic staining. As an alternate stain to Feulgen, 45min thionin showed the least variability and maximum stoichiometry among all the absorption stains. However, nuclear morphology was not well preserved, possibly because of high staining time, which might have caused over-staining and non-specific binding.

4.5 Conclusion

To conclude, more work has to be put into making OPTM quantitative for DNA content using fluorescent dye. Nonetheless, in its current state, it can be used to detect various fluorochrome labeled biomarkers for diagnosis of diseases, including cancer.

In extending DNA image cytometry from 2D to 3D, Feulgen stain still remains the gold standard compared to thionin, hematoxylin and sytox green. The 3D OPTM images of nuclei with Feulgen staining along with the automated algorithm of 3D nuclear segmentation demonstrated the ability to accurately measure DNA content concurrently with conventional morphological techniques extended to 3D.

Chapter 5: Testing stoichiometric DNA ploidy analysis with different cancer cell lines

In order to test that the current combined procedure of sample preparation, OPTM imaging and computational processing provides stoichiometric DNA ploidy, seven different cultured cancer cell lines were stained with Feulgen stain. Feulgen stain, which has been shown to be both stoichiometric as well as preserve morphology, should be able to accurately compute the DNA index of the individual cancer line. As usual, FCM was considered the reference, as it is currently the gold standard for aneuploidy measurement.

5.1 Sample preparation

Cultured human cancer cell lines of A549 (lung adenocarcinoma), BT474 (breast carcinoma), CaCO2 (colorectal adenocarcinoma), HepG2 (liver carcinoma), HT29 (colorectal adenocarcinoma), PC3 (prostate carcinoma), SKBR3 (breast adenocarcinoma) and NL 20 (normal human lung epithelial) from ATCC were used. Trout erythrocyte nuclei were used along with cancer cells on OPTM as an internal standard to determine the position of the diploid peak (2c). Human lymphocytes (HemaCare Corporation, USA) along with cancer cells were used to calculate the D.I of each cancer cell line using FCM.

5.2 Flow cytometry

Flow cytometry was performed in Dr Peter Rabinovitch laboratory, Department of Pathology, at University of Washington. Standard FCM was performed on all the seven cultured cancer cells and lymphocytes, which were fixed in 50% ethanol according to the conventional protocol and the manufacturer's instruction (50). Each sample was resuspended in an isotonic pH 7.4-buffered solution with 0.1% nonidet P-40 detergent, 10 μg/ml diamidino-2-phenylindole (DAPI) and 1% RNAse, triturated with a 26 gauge needle, and filtered through 40 mm steel mesh. The analysis was performed using an InFlux cytometer (BD Biosciences, USA) with UV excitation. A total of 20,000 cells were analyzed, and in all cases, a coefficient of variation (CV) below 4.0% was found. The DNA index and S-phase fraction (SPF) were analyzed for cancer cell in comparison with lymphocytes using the software program MultiCycle (Phoenix Flow Systems, San Diego, CA, USA) (51).

5.3 3D image cytometry

The cultured cancer cells along with TEN's were stained with feulgen stain as described in section 4.3.3 simultaneously. After preparing the sample and inserting the sample into the syringe, 100 images of each cancer cell and TEN were acquired and reconstructed as described in section 3.3 and 3.4 respectively. 3D segmentation of the nucleus from the cell using global threshold technique was performed as described previously in Figure 8. Note that the second peak was used as the threshold to segment out the nucleus as the first peak is used to segment out the cytoplasm from the background.

After 3D segmentation, all the voxels inside the nucleus were integrated to provide an IOD of the cancer cell as described in section 4.4. Similarly IOD of corresponding TEN were calculated and scaled to match the IOD of a normal human diploid cell. The ratios of these two IOD's gave the D.I of individual cancer cell line.

5.4 Results and Discussion

5.4.1 DNA index

The IOD's of TEN's were scaled and then used to transform the arbitrary unit scale of the cancer cells into a reference unit scale (2c, 4c, 6c etc). Correspondingly, DNA histograms were plotted and DNA indices were computed for each cancer cell. Figures 18-24 below show a comparison between histograms obtained from FCM and that obtained from OPTM.

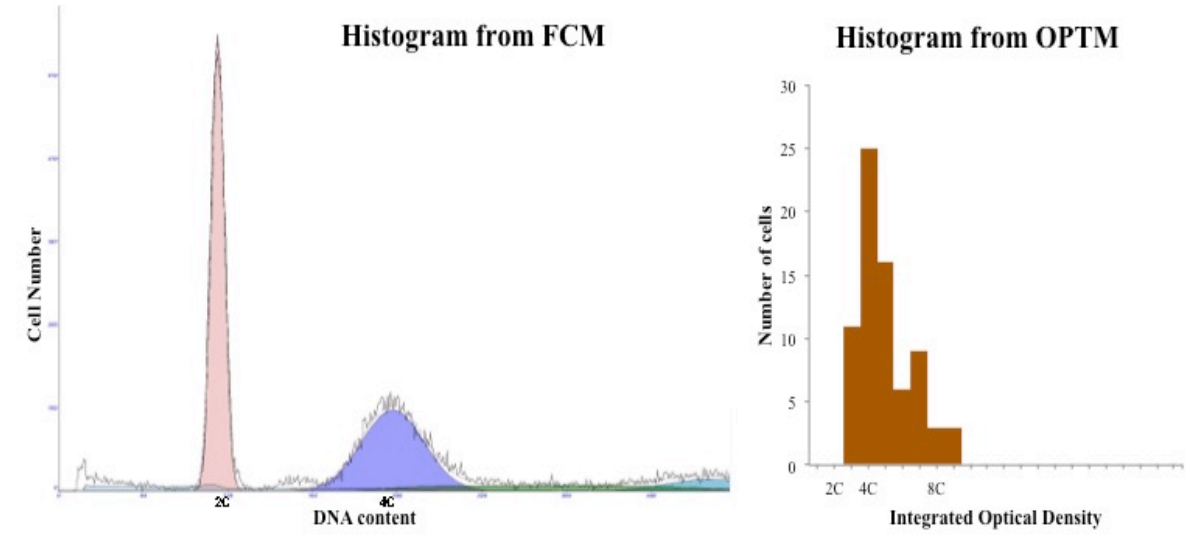

Fig 18. Comparison of histograms of PC3 from FCM and OPTM. Histogram from FCM contains both lymphocytes and cancer cells, while histogram from OPTM only has cancer cells. There was a good correlation between both the histograms as most of the cancer cells were concentrated around 4c region. The small green peak and the blue peak following the 4c in the FCM histogram corresponds to the S phase and the G2 phase of the tumour population.

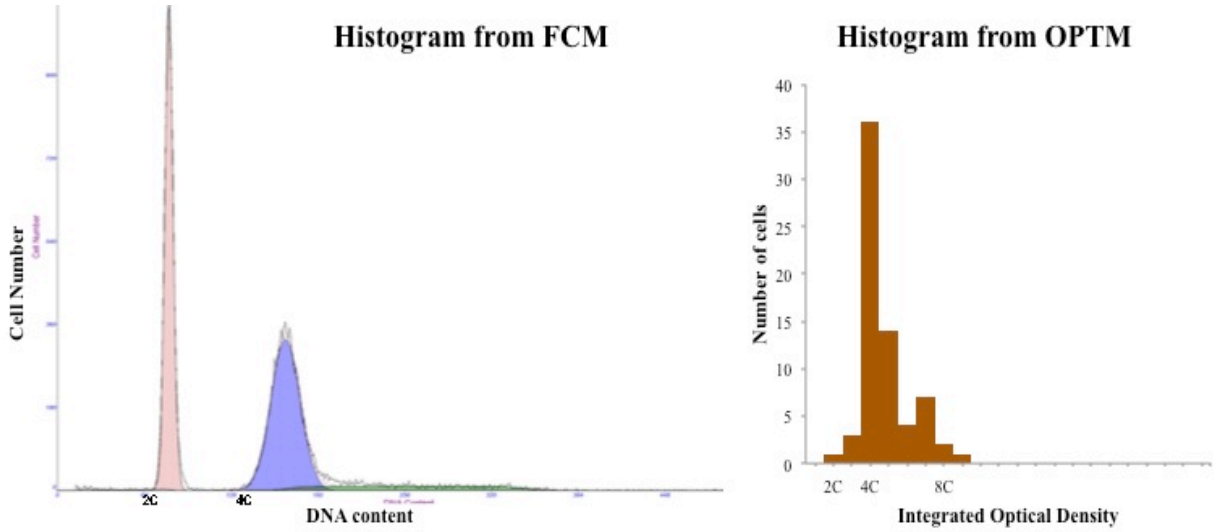

Fig 19. Comparison of histograms of HT29 from FCM and OPTM. Histogram from FCM contains both lymphocytes and cancer cells, while histogram from OPTM only has cancer cells. There was a good correlation between both the histograms as most of the cancer cells were concentrated after 4c region. The small green peak following aneuploidy peak in the FCM histogram corresponds to the S phase of the tumour population.

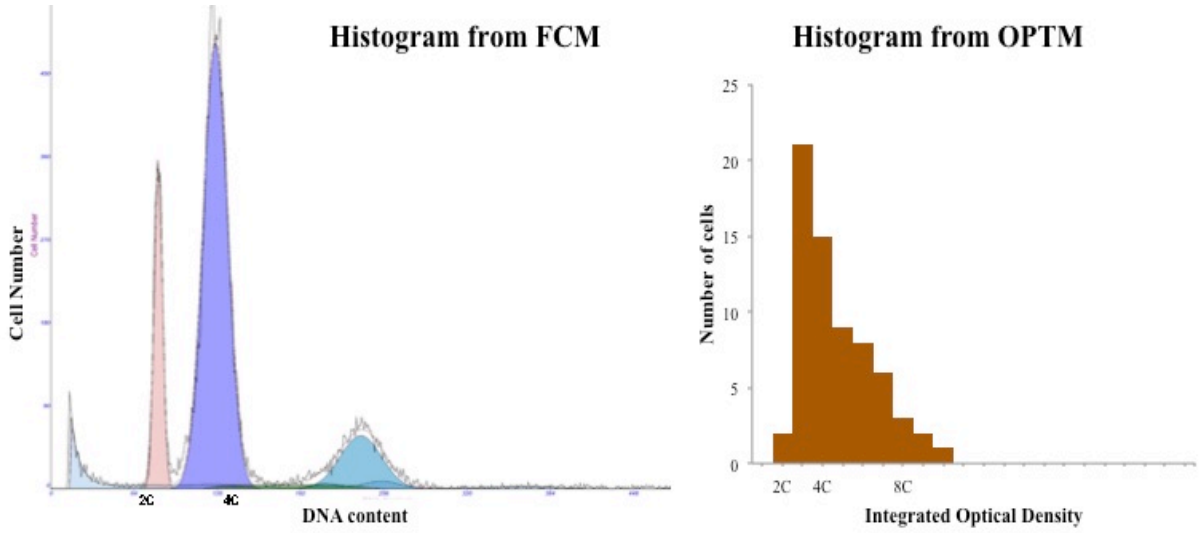

Fig 20. Comparison of histograms of HepG2 from FCM and OPTM. Histogram from FCM contains both lymphocytes and cancer cells, while histogram from OPTM only has cancer cells. There was a good correlation between both the histograms as most of the cancer cells were concentrated before 4c region. The small green peak and the blue peak following aneuploidy peak in the FCM histogram corresponds to the S phase and G2 phase of the tumour population.

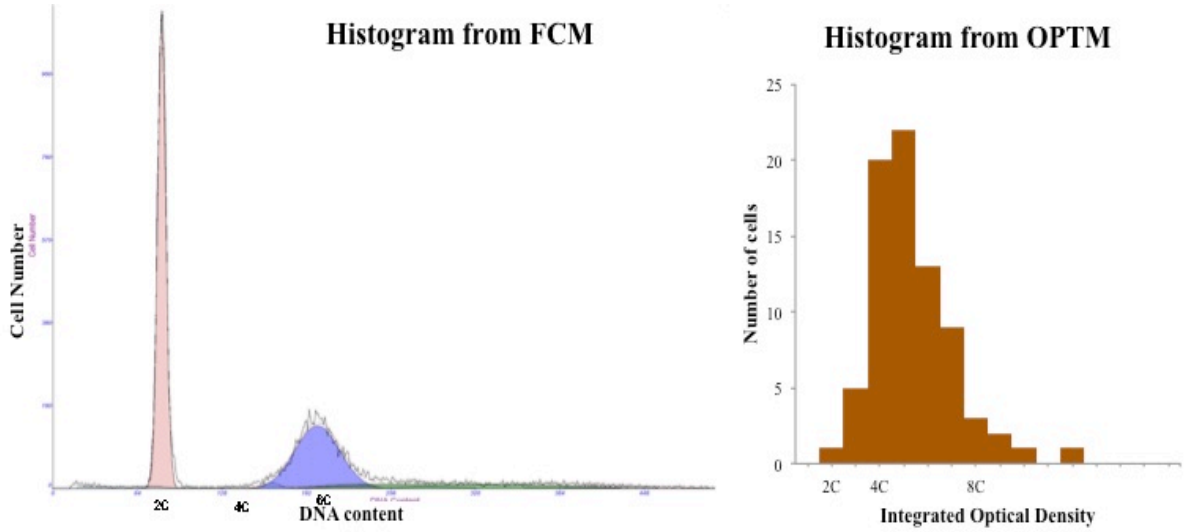

Fig 21. Comparison of histograms of CaCO2 from FCM and OPTM. Histogram from FCM contains both lymphocytes and cancer cells, while histogram from OPTM only has cancer cells. There was a good correlation between both the histograms as most of the cancer cells were concentrated at 6c region. The small green peak following aneuploidy peak in the FCM histogram corresponds to the S phase of the tumour population.

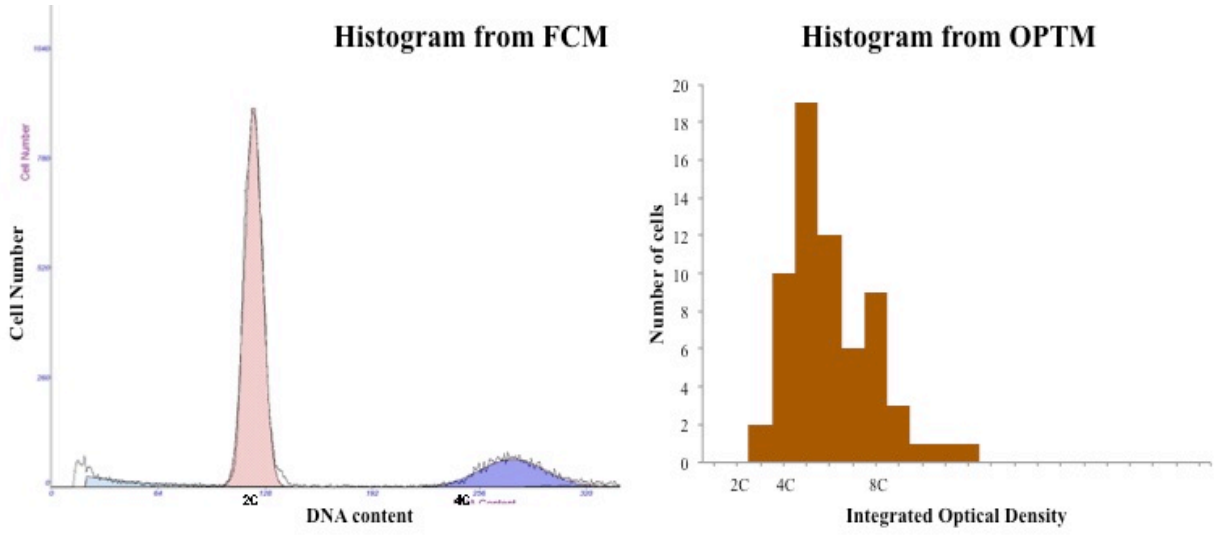

Fig 22. Comparison of histograms of SKBR3 from FCM and OPTM. Histogram from FCM contains both lymphocytes and cancer cells, while histogram from OPTM only has cancer cells. There was a good correlation between both the histograms as most of the cancer cells were concentrated after 4c region. The green peak following aneuploidy peak in the FCM histogram was removed for better visualization of the aneuploidy peak with lymphocytes.

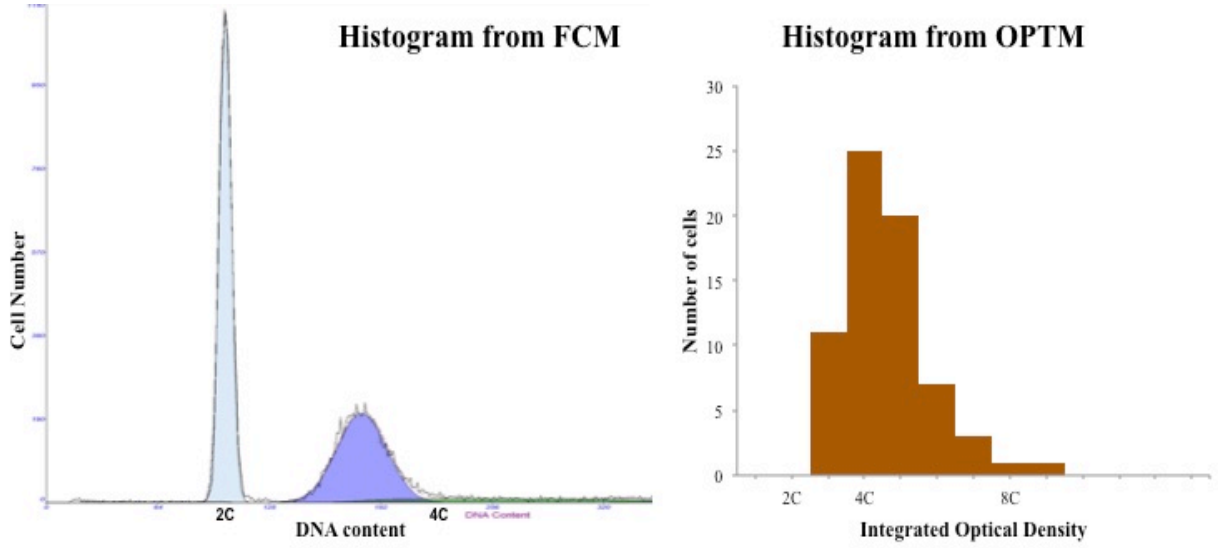

Fig 23. Comparison of histograms of A549 from FCM and OPTM. Histogram from FCM contains both lymphocytes and cancer cells, while histogram from OPTM only has cancer cells. There was not a good correlation between both the histograms as the aneuploidy peak in FCM histogram lied between 2c and 4c while the peak in histogram from OPTM was near 4c. The small green peak following aneuploidy peak in FCM histogram corresponds to the S phase of the tumour population.

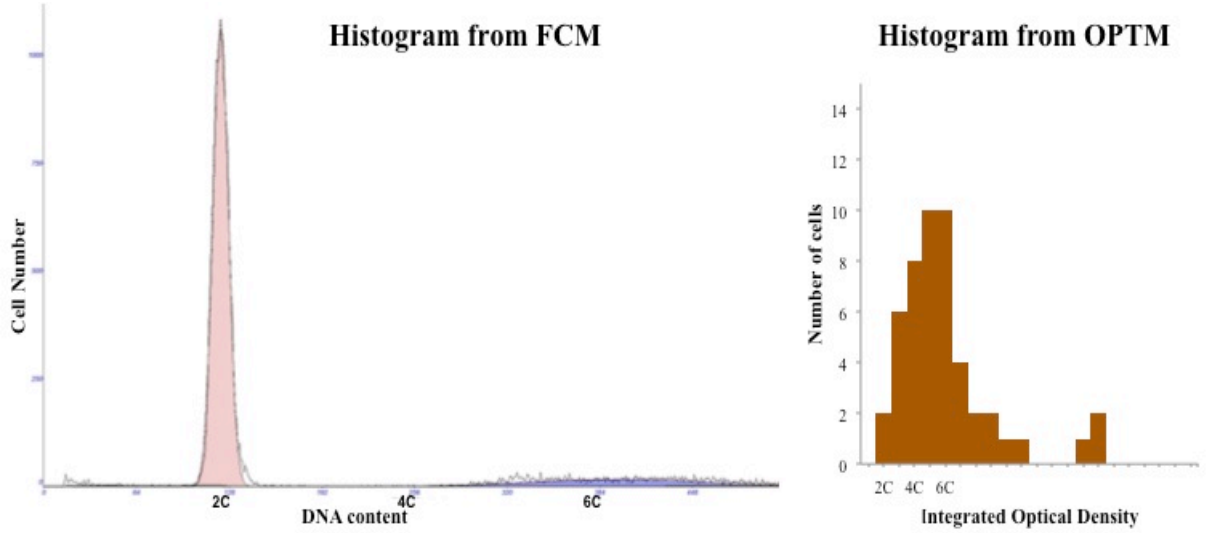

Fig 24. Comparison of histograms of BT474 from FCM and OPTM. Histogram from FCM contains both lymphocytes and cancer cells, while histogram from OPTM only has cancer cells. There was not a good correlation between both the histograms as the aneuploidy peak in FCM histogram was at 6c while the peak in histogram from OPTM was between 4c and 6c. The green peak following aneuploidy peak in FCM histogram was removed for better visualization of the tumour peak along with lymphocytes.

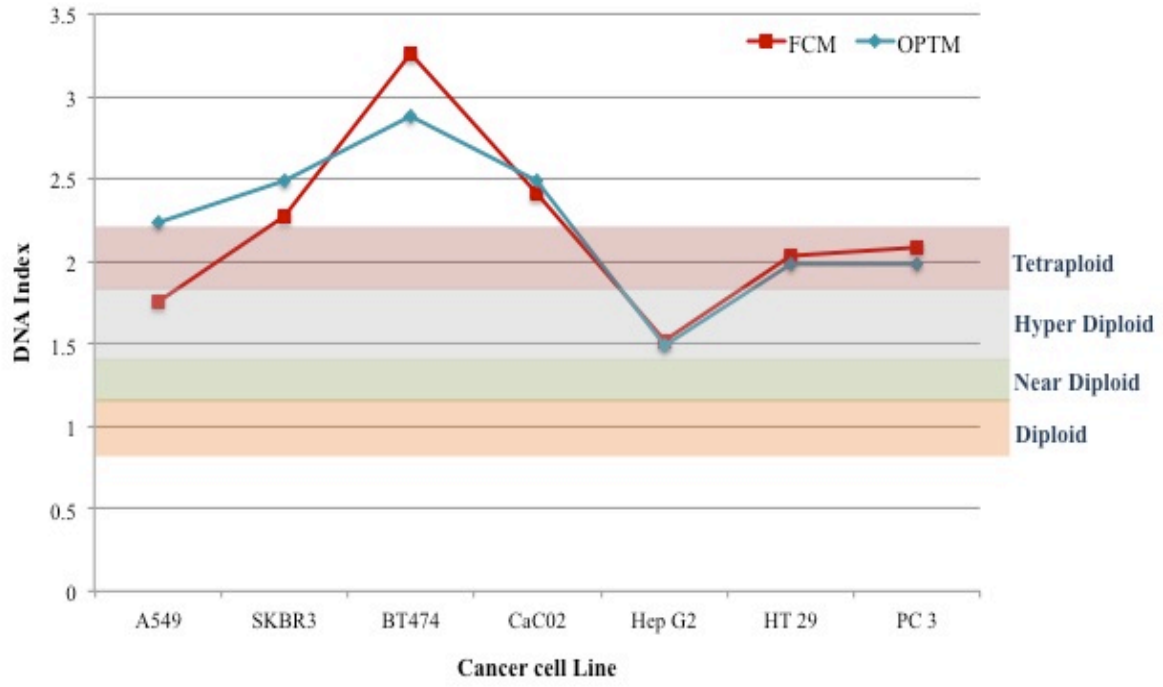

Fig 25. A comparison of DNA indices of seven different cancer cell lines from FCM and OPTM.

According to European Society for Analytical Cellular Pathology guidelines (ESACP) (46), a specimen is defined as diploid when there is only one peak (which was 2c, or DI = 0.9–1.1) during the G0 or G1 phase, when the number of 4c nuclei during the peak of the G2 phase has not exceeded 6% of the total, or when the number of nuclei with a DNA content of >5c has not exceeded 1% of the total. It is defined as DNA tetraploid when there is a population of 4C nuclei (DI = 1.9–2.1) >6% of the total, representing stage G2 of the cell cycle. It is defined as aneuploid when there is a population of nuclei with abnormal DNA content, separated from the diploid peak (DI >1.1), and representing >2.5% of the total or when the number of nuclei with a DNA content of >5c or 9c exceeded 1% of the total. Aneuploid cases are further divided into near-diploid aneuploid (1.1–1.29) and aneuploid (1.30–1.89) (65) as shown in Figure 25.

Classifying the seven cancer cells based on the classification from ESACP, since there was good concordance between FCM and OPTM for PC3, HT29, HepG2, CaCO2 and SKBR3 they are tetraploid, tetraploid, hyper diploid, pentaploid and pentaploid respectively. However A549 was hyper diploid from FCM and tetraploid from OPTM. Similar was the case with BT474, where there was a mismatch of DNA indices from FCM and OPTM (Table 2).

Cancer cell line	OPTM	FCM
PC 3	1.98	2.09
HT 29	1.98	2.03
Hep G2	1.49	1.52
CaC02	2.49	2.41
SKBR3	2.49	2.27
A549	2.24	1.76
BT474	2.88	3.26

Table 2. DNA indices of seven cancer cell lines from OPTM and FCM.

One of possible reasons for the different DNA indices between FCM and OPTM for A549 and BT474 was the 3D segmentation. It was observed that the global threshold technique used to segment out the nucleus of the cancer cells was not accurate (Figure 26). However it showed great results for perfectly circular or symmetrical objects like the standards used for calibration.

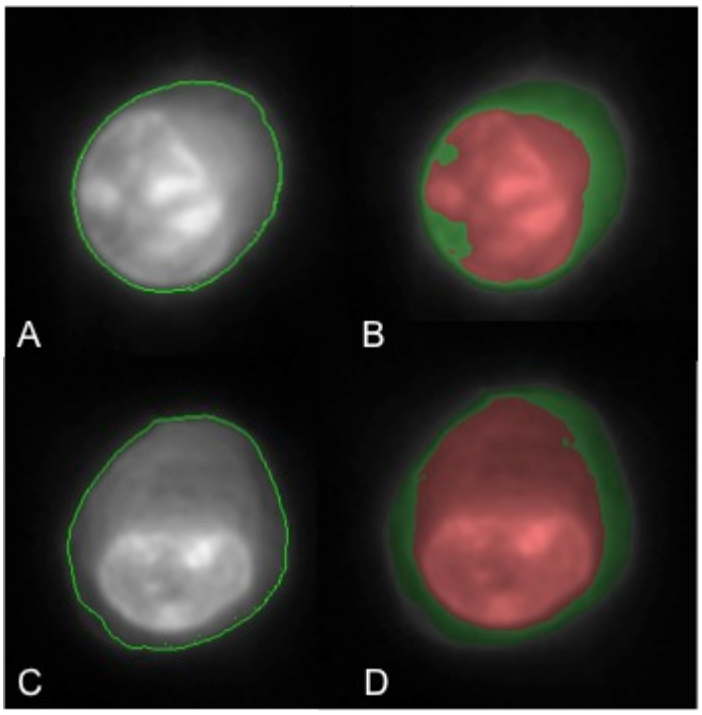

Fig 26. Performance of global threshold segmentation technique on A549 cancer cell line. (A) and (C) show the segmentation of cytoplasm on central slice of two different A549 cancer cells. (B) and (D) show the segmentation of both cytoplasm and nucleus on central slice of the same cancer cells.

Another possible reason for this disagreement could be errors in the OPTM system. There were many assumptions taken while computing the DNA index of the sample. It was assumed that the rays falling on the specimen were parallel, however due to the high NA of the condenser and the objective the illumination was non-collimated. Further, it had also been proven that the sample does not show 100% absorption. There is partial refraction (66) as well, due to which a modified beer lamberts law might be required for calculations. Further during image acquisition, the focal plane of the condenser was stationary while the focal plane of the objective scans the specimen

axially (66). This causes artifacts during 3D reconstruction, which could have also been one of the reasons for this disparity between the DNA indices. It had also been shown that there is incomplete scanning of the specimen by the objective resulting in having incomplete 3D reconstruction of the specimen. This would indirectly affect the nuclear volume and hence the DNA index. It was due to these systems errors, that ratios of DNA indices were taken into considerations rather than absolute values.

Figure 27 shows a plot of the coefficient of variation (CV) of TEN computed by FCM and OPTM. It was observed that OPTM gave an average CV of 10% as against FCM, which showed 4%. This suggests that OPTM currently has a high standard deviation when calculating DNA indices as against FCM.

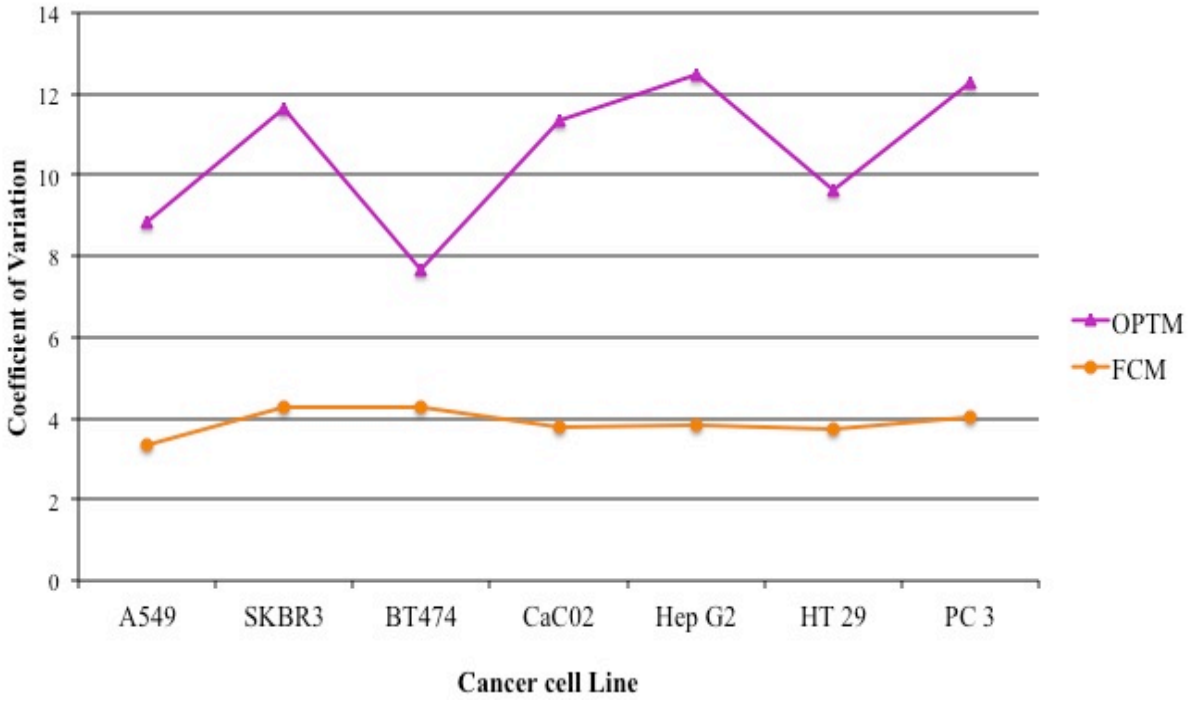

Fig 27. Comparison of coefficient of variations of TEN between OPTM and FCM.

5.4.2 S-phase fraction

The SPF of each cancer cell lines was computed by FCM as shown in Table 3.

CANCER CELL LINE	SPF
A549 (human lung adenocarcinoma)	17.63%
SKBR 3 (human breast adenocarcinoma)	25.06%
BT474 (human breast carcinoma)	16.62%
CaCO2 (human colorectal adenocarcinoma)	24.65%
HepG2 (human liver carcinoma)	3.48%
HT 29 (human colorectal adenocarcinoma)	16.27%
PC 3 (human prostate carcinoma)	18%

Table 3. Table representing SPF values of different cancer cell lines.

SPF values are more accurate for FCM than ICM as FCM analyses a much more bigger sample size to evaluate the SPF than ICM.

5.4.3 Morphology

Morphology was preserved for all the cancer cell lines stained with feulgen stained (Figure 28). Further the morphology of an A549 lung cancer cell was compared with that of NL20, a normal human lung epithelial cell line and distinct differences were observed (Figure 29).

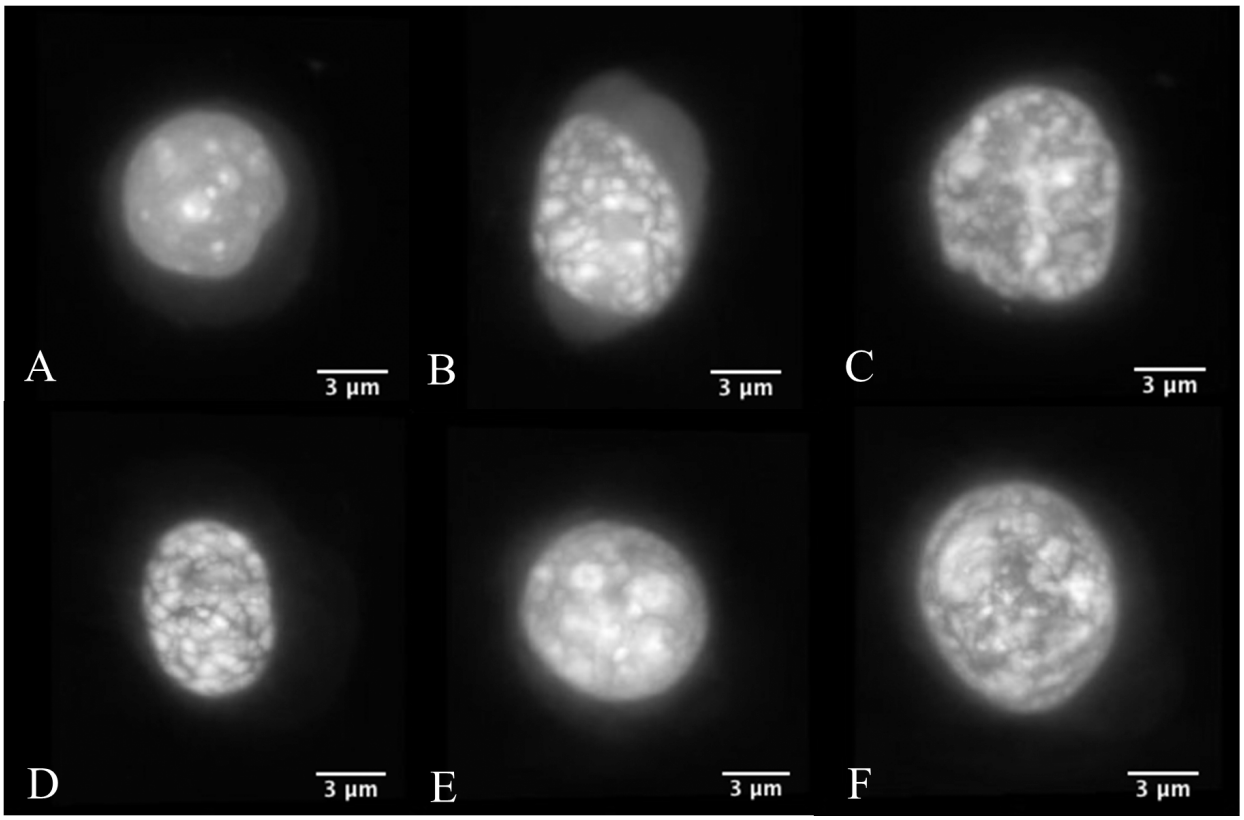

Fig 28. 3D axial views of (A). CacO2 cell (human colorectal adenocarcinoma), (B). HepG2 cell (human liver carcinoma), (C). HT29 cell (human colorectal adenocarcinoma), (D). PC3 cell (human prostate carcinoma), (E). SKBR3 cell (human breast adenocarcinoma) and (F). BT474 cell (human breast carcinoma) stained with Feulgen stain.

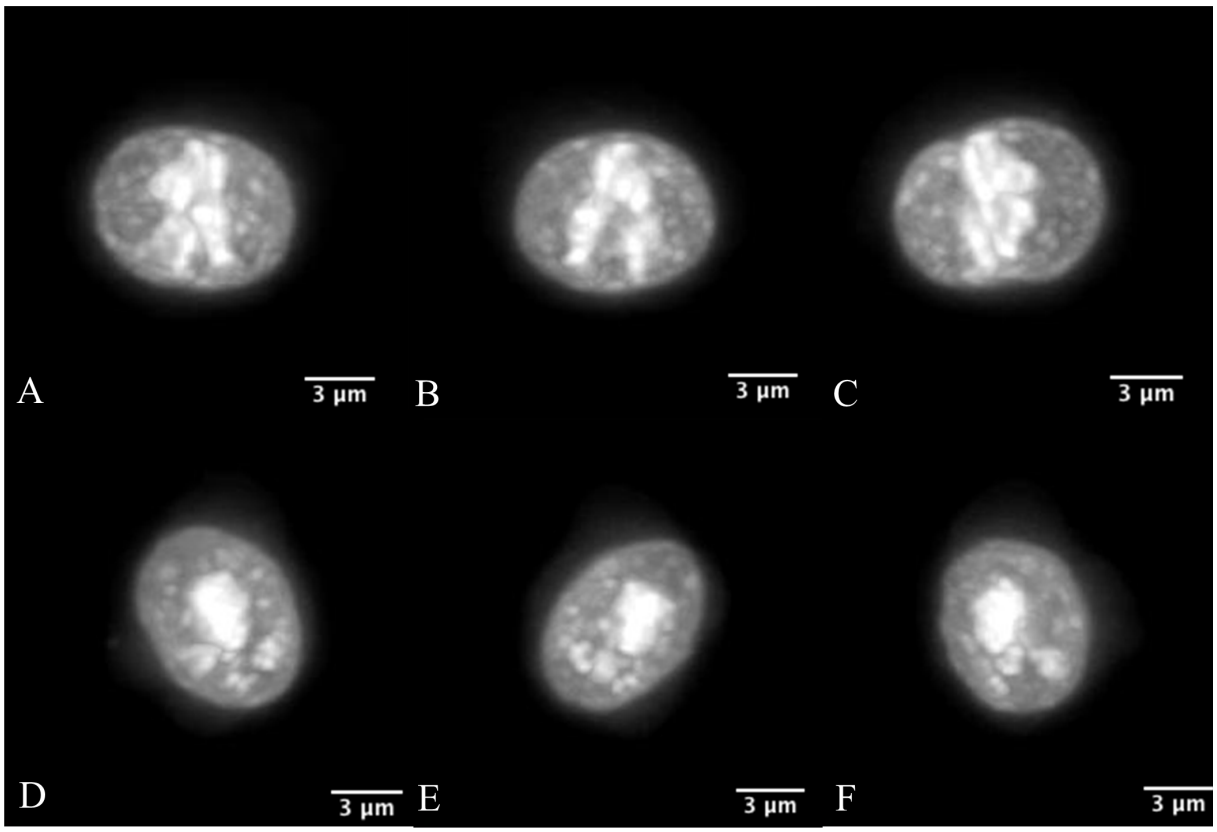

Fig 29. 3D images of (A). axial, (B). sagittal and (C). coronal views of an A549 cell (human lung adenocarcinoma) in comparison with 3D images of (D). axial, (E). sagittal and (F). coronal views of NL 20 (normal human lung epithelial cell) stained with Feulgen stain. The nuclear morphology of a cancer cell is distinguishable from a normal cell from culture. NL20 has dense concentrated chromatin content while A549 has a much more complex and heterogeneous chromatin content.

5.5 Conclusion

Feulgen stain showed accurate DNA index assessment for all the seven cancer cell lines except A549 and BT474. Differences in DNA indices of both these cancer cell lines could be explained by inaccurate 3D segmentation and system errors.

Morphology of all the cancer cell lines was preserved with feulgen stain. Distinct 3D morphological features were seen between A549 (lung adenocarcinoma) and NL 20 (normal

human lung epithelial), suggesting that in future it can be also used as a biomarker for early cancer diagnosis.

Chapter 6: Future directions and Conclusion

6.1 Clinical Impact

OPTM is a technique through which we can obtain 3D information of single cells. VisionGate, a small start-up company based in phoenix has commercialized this as Cell-CT (67). VisionGate uses the Cell-CT to build classifiers based on 3D features for early lung cancer diagnosis (68). Our technique of stoichiometric DNA ploidy analysis could strengthen existing classifiers for diagnosis of lung cancer at an early stage.

Sputum samples generally contain only 1% of respiratory epithelial cells and rest are squamous cells, macrophages and debris (69). Of these 1% epithelial cells, very few are cancer cells. This sample if run on an FCM would not be able to give accurate DNA ploidy assessment. However, accurate DNA ploidy analysis could be achieved using OPTM.

VisionGate basically enrich induced sputum samples for respiratory epithelial cells. They then stain it with hematoxylin and image it using Cell-CT. Various classifiers are then run over the sample to analyze whether the original sample had cancer cells or not. The addition of our technique of quantitative DNA ploidy assessment in combination with existing biomarkers would strengthens the existing classifiers for an improved lung cancer diagnosis.

6.2 Improved OPTM

For DNA ploidy analysis, we had used a second generation Cell-CT and had made many approximations like the specimen being 100% absorptive, parallel illumination etc. Most of these issues have been addressed in the newer generations of the Cell-CT manufactured by VisionGate.

Further, inspite of having high sensitivity and specificity, one of the biggest limitations of Cell-CT is its low throughput. Though VisionGate has made substantial improvements in increasing the throughput to nearly 1 cell per second (30 times more than the second generation), even greater improvements in throughput are probably necessary for it to compete with the existing devices in the market.

6.3 Improved 3D segmentation

It was observed that the global thresholding technique used for 3D segmentation of nuclei was accurate for perfectly symmetrical or circular objects like the internal standards or lymphocytes, but not for irregular shaped structures like the cancer cells. It sometimes segmented a greater region than the actual nuclei and sometimes less as shown in Figure 26.

The computer vision and analysis group at Cornell University has recently developed a new technique for accurate 3D segmentation. Graph cut using convex hull has showed far superior performance than the traditional global thresholding technique especially for irregular shaped objects like the cancer cells (Figure 30). This segmentation algorithm is far more complicated and adaptive than global thresholding technique in which after applying graph cut segmentation, a convex hull algorithm is used to predict and complete the boundaries of the 3D segmented nuclei.

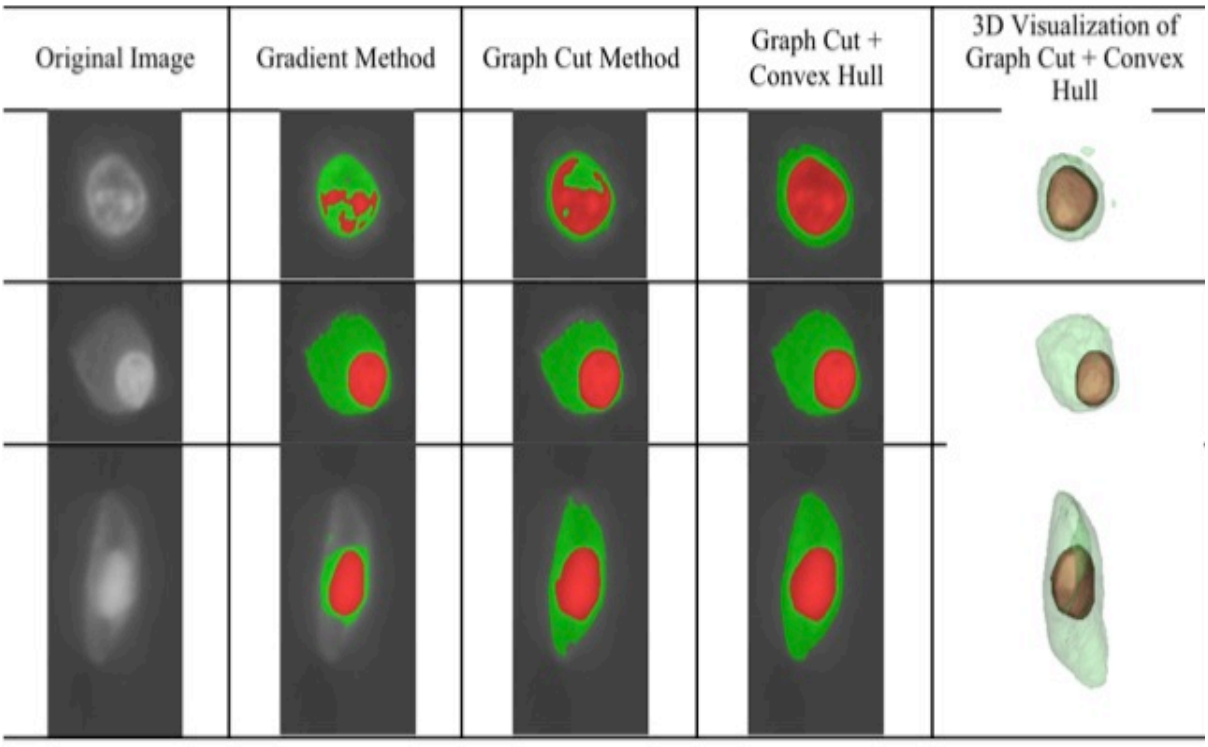

Fig 30. Performance of three different 3D segmentation algorithms used on cancer cells. The left most column shows central slice of the cancer cell followed by segmentation of that cancer cell using gradient method, followed by segmentation of that cancer cell using graph cuts methods, followed by segmentation of that cancer cell using graph cut with convex hull algorithm and finally 3D visualization of cancer cells using graph cut and convex hull to the far right.

Using this new 3D segmentation technique we plan on reanalysing the data for cancer cells and hope to achieve better accuracy for DNA indices, especially for A549 and BT474. It was also observed that in A549 there were more number of nuclei having bigger segmented regions than number of nuclei having lesser segmented regions. However, the case was totally reverse for BT474. This could be a probable reason for DNA index of A549 to be greater with OPTM than FCM and DNA index of BT474 to be less with OPTM than FCM. Using this improved 3D segmentation we hope to achieve accurate 3D segmentation, in which both these types of error would be reduced. This would not only result in good correlation with FCM but also would potentially reduce the CV of OPTM as against FCM (Figure 27).

6.4 Tissue Biopsies Analysis

Apart from doing single cell analysis, another possible future of OPTM could be analysing tissue samples (70). Tissue biopsies taken by pathologist for diagnosis are very common in cytology. They take biopsies and then later view them under bright field microscope. Just like cytotechnician who look at characteristics of individual cells, pathologist look at gross morphology of the tissue. The advantage of analysing tissue samples is that sometimes for some cancers it gives far more information than analysing single cells. Due to this pathologist sometimes prefer analysing tissue samples to single cells.

As with single cells analyses, there are a number of scientific and technical problems that need to be addressed before using OPTM for tissue sample analysis. Scattering of light, the sample being very large and preparation of the sample for OPTM imaging are some of the problems, which make OPTM quite difficult for tissue analyses.

6.5 Conclusion

In this study we have successfully performed 3D DNA image cytometry using optical projection tomographic microscopy for early cancer diagnosis. This is the first study that has quantitatively measured DNA content in 3D using absorption stains for cancer diagnosis. OPTM is an imaging flow cytometer, which combines few of the benefits of both image as well as flow cytometry. It is superior to traditional image cytometers as they are all two-dimensional and is ideal for small population samples unlike flow cytometer, which are ideal for large population samples.

Using OPTM, we have shown that feulgen stain is the most accurate, least variable stain in terms of stoichiometry and also preserves nuclear morphology in 3D. Further hematoxylin stain, the most common stain used in cytology is not at all stoichiometric and has high variance, inspite of

preserving nuclear morphology. Acidic thionin stain, which was stoichiometric and preserved nuclear morphology in 2D, showed good stoichiometry but did not preserve nuclear morphology in 3D. We also performed quantitative DNA content analysis using sytox green, a fluorescent stain and showed that it is more stoichiometric than hematoxylin but less than acidic thionin and feulgen stain. More work has to be put into making OPTM quantitative for DNA content using fluorescent dye. Nonetheless, in its current state, it can be used for quantitative DNA ploidy assessment using absorption stains along with detection of various fluorochrome labeled biomarkers for diagnosis of various diseases, including cancer.

We further tested out feulgen stain on different cancer cell lines and obtained good correlation with flow cytometry, which is currently considered the gold standard for aneuploidy. However there was a mismatch of DNA index between two cancer cell lines, A549 and BT474.

We also developed a novel algorithm using global thresholding technique for 3D segmentation of nuclei from a cell. We further observed that this algorithm showed superior performance with symmetrical or circular objects, but failed to segment irregular shaped objects, seen more often with A549 cancer cell line. We have also proposed to reanalyse the data for cancer cells using an improved segmentation algorithm, which uses graph cuts algorithms with convex hull.

Hence, aneuploidy or quantitative DNA content assessment is a biomarker, which can be integrated into the Cell-CT to strengthen existing classifiers for early lung cancer diagnosis.

References

1. Fonseca R, Hartmann LC, Petersen IA. Ductal carcinoma in situ of the breast. Ann Intern Med 127 (11): 1013-22, 1997.
2. Esserman L, Shieh Y, Thompson I. Rethinking Screening for Breast Cancer and Prostate Cancer. JAMA. 302(15):1685-1692, 2009.
3. World Heath Organization. http://www.who.int/mediacentre/factsheets/fs297/en/index.html.
4. Neiburg H. Diagnostic cell pathology in tissue and smears. New York: Grune & Stratton, Inc, 1967.
5. Reeves AP, Seibel EJ, Meyer MG, Apanasovich T, Biancardi A. Nuclear cytoplasmic cell evaluation from 3D optical CT microscope images. Proc. SPIE 8315:83153C, 2012.
6. Atkin NB. Modal deoxyribonucleic acid value and survival in carcinoma of the breast. Br Med J 1:271–272, 1972.
7. Atkin NB, Kay R. Prognostic significance of modal DNA value and other factors in malignant tumors, based on 1465 cases. Br. J. Cancer 40:210–221, 1979.
8. Atkin NB, Mattinson G, Baker MC. A comparison of the DNA content and chromosome number of fifty human tumours. Br. J. Cancer 20:87, 1966.
9. Fang M, Lew W, Klein M, Sebo T, Su Y, Goyal R. DNA abnormalities as marker of risk for progression of Barrett's esophagus to adenocarcinoma: image cytometric DNA analysis in formalin-fixed tissues. Am J Gastroenterology 99(10):1887–94, 2004.
10. Schmidt D, Wischmeyer P, Leuschner I, Sprenger E, Langenau E, Schweinitz DV, Harms D. DNA analysis in hepatoblastoma by flow and image cytometry. Cancer 72(10):2914–2919, 1993.
11. Huang Q, Yu C, Klein M, Fang J, Goyal RK. DNA index determination with Automated Cellular Imaging System (ACIS) in Barrett's esophagus: comparison with CAS 200. BMC Clin Pathol 5:7, 2005.
12. Santos-Silva AR, Ribeiro ACP, Soubhia AMP, Miyahara GI, Carlos R, Speight PM, Hunter KD, Torres-Rendon A, Vargas PA, Lopes MA. High incidences of DNA ploidy abnormalities in tongue squamous cell carcinoma of young patients: an international collaborative study. Histopathology 58:1127–1135, 2011.

13. Kreicbergs A, Broström LA, Cewrien G, Einhorn S. Cellular DNA content in human osteosarcoma: aspects on diagnosis and prognosis. Cancer 50:2476–2481, 1982.
14. Haroske G, Baak JP, Danielsen H, Giroud F, Gschwendtner A, Oberholzer M, Reith A, Spieler P, Böcking A. Fourth updated ESACP consensus report on diagnostic DNA image cytometry. In: Anal Cell Pathol. 23:89–95, 2001.
15. Joensuu H, Toikkanen S, Klemi PJ. DNA index and S-phase fraction and their combination as prognostic factors in operable ductal breast carcinoma. Cancer 66:331–340, 1990.
16. O'Reilly SM, Camplejohn RS, Barnes DM, Millis RR, Allen D, Rubens RD, Richards MA. DNA index, S-phase fraction, histological grade and prognosis in breast cancer. Br. J. Cancer 61:671–674, 1990.
17. Spyratos F, Briffod M. DNA ploidy and S-phase fraction by image and flow cytometry in breast cancer fine-needle cytopunctures. Mod. Pathol. 10:556–563, 1997.
18. Carrillo R, Candia A, Rodriguez-Peralto JL, Caz V. Prognostic significance of DNA ploidy and proliferative index (MIB-1 index) in gastrointestinal stromal tumors. Hum. Pathol. 28:160–165, 1997.
19. Luzi PP, Bruni AA, Mangiavacchi PP, Cevenini GG, Marini DD, Tosi PP. Ploidy pattern and cell cycle in breast cancer as detected by image analysis and flow cytometry. Cytometry 18:79–87, 1994.
20. Hedley DW, Rugg CA, Gelber RD. Association of DNA index and S-phase fraction with prognosis of nodes positive early breast cancer. Cancer Res 47:4729–4735, 1987.
21. Dawson AE, Norton JA, Weinberg DS. Comparative assessment of proliferation and DNA content in breast carcinoma by image analysis and flow cytometry. Am. J. Pathol. 136:1115–1124, 1990.
22. Rosenberg P, Wingren S, Simonsen E, Stàl O, Risberg B, Nordenskjöld B. Flow cytometric measurements of DNA index and S-phase on paraffin-embedded early stage endometrial cancer: an important prognostic indicator. Gynecol. Oncol. 35:50–54, 1989.
23. Ellison DA, Maygarden SJ, Novotny DB. Quantitative DNA analysis of fresh solid tumors by flow and image cytometric methods: a comparison using the Roche Pathology Workstation Image Analyzer. Mod. Pathol. 8:275– 281, 1995.

24. Pindur A, Chakraborty S, Welch DG, Wheeler TM. DNA ploidy measurements in prostate cancer: Differences between image analysis and flow cytometry and clinical implications. Prostate 25:189–198, 1994.
25. Alanen KA, Lintu M, Joensuu H. Image cytometry of breast carcinomas that are DNA diploid by flow cytometry: time to revise the concept of DNA diploidy? Anal. Quant. Cytol. Histol. 20(3) 178-186, 1998.
26. Dunn JM, Mackenzie GD, Oukrif D, Mosse CA, Banks MR, Thorpe S, Sasieni P, Bown SG, Novelli MR, Rabinovitch PS, Lovat LB. Image cytometry accurately detects DNA ploidy abnormalities and predicts late relapse to high-grade dysplasia and adenocarcinoma in Barrett's esophagus following photodynamic therapy. Br. J. Cancer 102:1608– 1617, 2010.
27. Partec. http://www.partec.com/company/flow-museum/icp-11-1968.html.
28. Schulte E, Wittekind D. Standardization of the Papanicolaou stain. I. A comparison of five nuclear stains. Anal. Quant. Cytol. Histol. 12:149, 1990.
29. Oud, PS, Zahniser DJ, Vooijs GP, Raaymakers MC, van de Walle RT. Thionine-Feulgen Congo Red - a new staining technique for automated cytology. Acta Histochem. Suppl. 24:199–206, 1981.
30. Haour P, Conti C. Advantages and disadvantages of the Feulgen reaction and histophotometric technique as applied to cervical smears. Acta Cytol 2:326 326-327, 1958.
31. Schulte E, Wittekind D. Standardized thionin-eosin stain in bronchial cytology. A substitute for hematoxylin-eosin Y staining. Anal. Quant. Cytol. Histol. 11:131–139, 1989.
32. Schulte EK, Wittekind DH. Standardized thionin-eosin Y: a quick stain for cytology. Stain Technol. 64:255–256, 1989.
33. Wittekind D, Reinhardt ER, Kretschmer V, Zipfel E. Influence of staining on fast-automated cell segmentation, feature extraction and cell image analysis. Analyt Quant Cytol. 5:55-60, 1983.
34. Sharpe J. Optical Projection Tomography as a Tool for 3D Microscopy and Gene Expression Studies. Science 296:541–545, 2002.

35. Alanentalo T, Asayesh A, Morrison H, Lorén CE, Holmberg D, Sharpe J, Ahlgren U. Tomographic molecular imaging and 3D quantification within adult mouse organs. Nat Meth. 4:31–33, 2007.
36. Oldham M, Sakhalkar H, Wang YM, Guo P, Oliver T, Bentley R, Vujaskovic Z, Dewhirst M. Three-dimensional imaging of whole rodent organs using optical computed and emission tomography. J Biomed Opt. 12:014009, 2007.
37. Pampaloni F, Reynaud EG, Stelzer EHK. The third dimension bridges the gap between cell culture and live tissue. Nat. Rev. Mol. Cell Biol. 8:839–845, 2007.
38. D Huang, EA Swanson, CP Lin, JS schuman, WG Stinson, W Change, MR Hee, T Flotte, K Gregory, CA Puliafito, Science 254 (5035), 1178-1181, 1991.
39. Z. Yuan and H. Jiang, Three-dimensional finite-element-based photoacoustic tomography: Reconstruction algorithm and simulations," Medical Physics 34, 538, 2007.
40. Garini Y, Vermolen BJ, Young IT. From micro to nano: recent advances in high-resolution microscopy. Curr. Opin. Biotechnol. 16:3–12, 2005.
41. Fronheiser M, Ermilov SA, Brecht H, Su R, Conjusteau A, Oraevsky AA. Whole-body three-dimensional optoacoustic tomography system for small animals. J Biomed Opt. 14:064007, 2009.
42. Wilson T, Confocal microscopy, London: Academic Press, 1990.
43. Meyer MG, Fauver M, Rahn JR, Neumann T, Patten FW, Seibel EJ, Nelson AC. Automated cell analysis in 2D and 3D: A comparative study. Pattern Recognition 42:141–146, 2009.
44. Fauver M, Seibel E, Rahn JR, Meyer M, Patten F, Neumann T, Nelson A. Three-dimensional imaging of single isolated cell nuclei using optical projection tomography. Opt Express 13:4210–4223, 2005.
45. Miao Q, Reeves AP, Patten FW, Seibel EJ. Multimodal 3D Imaging of Cells and Tissue, Bridging the Gap Between Clinical and Research Microscopy. Ann Biomed Eng. 40:263–276, 2011.
46. Böcking A, Giroud F, Reith A. Consensus report of the ESACP task force on standardization of diagnostic DNA image cytometry. Anal Cell Pathol. 8:67–74, 1995.
47. Allison RT, Sanders HA. Thionin: spectrophotometry and thin-layer chromatography in relation to biological staining. Med Lab Sci. 42:213–220, 1985.

48. Deriche R. Using Canny's criteria to derive a recursively implemented optimal edge detector. International journal of computer vision 1:167–187, 1987.
49. Monga O, Deriche R, Rocchisani J-M. 3D edge detection using recursive filtering: Application to scanner images. CVGIP: Image Understanding 53:76–87, 1991.
50. Flow Cytometry Facility, The Rabinovitch laboratory, Dept of Pathology, University of Washington. http://www.pathology.washington.edu/research/labs/rabinovitch/flowroom/protocols.php?p=1.
51. Rabinovitch PS. DNA content histogram and cell-cycle analysis. Methods Cell Biol. 41:263–296, 1994.
52. Zahniser, D.J., Lapen, D.C., Oud, P.S., "Thionin staining and imaging technique," US patent number: 5168066, issue date Dec 11992.
53. Schulte EK. Standardization of the Feulgen reaction for absorption DNA image cytometry: a review. Anal Cell Pathol. 3:167, 1991.
54. Schulte EK, Wittekind DH. Standardization of the Feulgen reaction: the influence of chromatin condensation on the kinetics of acid hydrolysis. Anal Cell Pathol. 2:149–157, 1990.
55. Schulte E, Wittekind D. Standardization of the Feulgen-Schiff technique. Staining characteristics of pure fuchsin dyes; a cytophotometric investigation. Histochemistry 91:321–331, 1989.
56. Feulgen R, Rossenbeck H. Mikroskopisch-chemischer Nachweis einer Nukleinsäure von Typus der Thymonuklein- säure und die darauf beruhende selektive Färbung von Zellkernen in mikroskopischen Präparaten. Hoppe-Seylers Z Physiol Chem. 135:203-248, 1924.
57. Reeves AP. Cornel university vision and image analysis group. http://www.via.cornell.edu/visionx/.
58. Miller RG. Simultaneous statistical inference. 2nd ed. New York: Springer Verlag; p6-8, 1981.
59. Marcello P, and Kimberlee G. Principles of Biostatistics. California: Wadsworth Publishing Company; p 263- 265, 1993.

60. Mendonca MAC, Carvalho CR, Clarindo WR. DNA Content Differences Between Male and Female Chicken (Gallus gallus domesticus) Nuclei and Z and W Chromosomes Resolved by Image Cytometry. Journal of Histochemistry & Cytochemistry 58:229–235, 2010.
61. Vindeløv LL, Christensen IJ, Nissen NI. Standardization of high-resolution flow cytometric DNA analysis by the simultaneous use of chicken and trout red blood cells as internal reference standards. Cytometry 3:328–331, 1983.
62. Chieco P, Derenzini M. The Feulgen reaction 75 years on. Histochem. Cell Biol. 111:345–358, 1999.
63. Biesterfeld S, Beckers S, Del Carmen Villa Cadenas M, Schramm M. Feulgen staining remains the gold standard for precise DNA image cytometry. Anticancer Res. 31:53–58, 2011.
64. Gurley AM, Hidvegi DF, Bacus JW, Bacus SS. Comparison of the Papanicolaou and Feulgen staining methods for DNA quantification by image analysis. Cytometry 11:468–474, 1990.
65. Lindahl B, Ranstam J, Willen R. Five year survival rate in endometrial carcinoma stages I – II: influence of degree of tumour differentiation, age, myometrial invasion and DNA content. Br J Obstet Gynaecol. 101:621–625, 1990.
66. Coe RL, Seibel EJ. Experimental and theoretical analysis for improved microscope design of Optical Projection Tomographic Microscopy. Opt. Lett. 38(17):3398-3401, 2013.
67. Cell-CT, VisionGate Inc. www.visiongate3d.com.
68. Nelson A, Meyer M, Neumann T, Hayenga J, Katdare R, Presley C, Hawthorne B, Steinhauer D, Bell T, Spring S, et al. Non-invasive Detection of Lung Cancer from Cells in Sputum Using Cell-CTTM. IASLC 2013 (abstract in press).
69. Kraemer PS, Sanchez CA, Goodman GE, Jett J, Rabinovitch PS, Reid BJ. Flow cytometric enrichment for respiratory epithelial cells in sputum. Cytometry A 60:1–7, 2004.

70. Chou KF, Miao Q, Coe RL, Seibel EJ. 3D Imaging of Fine Needle Aspirates Using Optical Projection Tomographic Microscopy. J Cytol. Histol. doi: 10.4172/2157-7099 S2: 001, 2012.